

---

# Your diffusion model secretly knows the dimension of the data manifold

---

**Jan Stanczuk \***

University of Cambridge  
Cambridge CB3 0WA  
js2164@cam.ac.uk

**Georgios Batzolis \***

University of Cambridge  
Cambridge CB3 0WA  
gb511@cam.ac.uk

**Teo Deveney**

University of Bath  
Bath BA2 7AY  
T.J.Deveney@bath.ac.uk

**Carola-Bibiane Schönlieb**

University of Cambridge  
Cambridge CB3 0WA  
cbs31@cam.ac.uk

## Abstract

In this work, we propose a novel framework for estimating the dimension of the data manifold using a trained diffusion model. A diffusion model approximates the score function i.e. the gradient of the log density of a noise-corrupted version of the target distribution for varying levels of corruption. We prove that, if the data concentrates around a manifold embedded in the high-dimensional ambient space, then as the level of corruption decreases, the score function points towards the manifold, as this direction becomes the direction of maximal likelihood increase. Therefore, for small levels of corruption, the diffusion model provides us with access to an approximation of the normal bundle of the data manifold. This allows us to estimate the dimension of the tangent space, thus, the intrinsic dimension of the data manifold. To the best of our knowledge, our method is the first estimator of the data manifold dimension based on diffusion models and it outperforms well established statistical estimators in controlled experiments on both Euclidean and image data.

## 1 Introduction

Many modern real-world datasets contain a large number of variables, often exceeding the number of observations. This poses a major challenge in modelling them, due to the *curse of dimensionality*. However, despite this complexity, such data often concentrates around a lower-dimensional manifold, a concept known as the *manifold hypothesis* Fefferman et al. [2013]. This hypothesis has guided the development of modern high-dimensional data modeling techniques like GANs Goodfellow et al. [2014] and VAEs Kingma and Welling [2013], as well as dimensionality reduction methods such as PCA Pearson [1901] and t-SNE Hinton and Roweis [2002]. These approaches require knowledge of the data’s intrinsic dimension, a critical hyperparameter.

In this work, we introduce a novel method, which estimates the dimension of the data manifold by leveraging information contained in a trained diffusion model.

Diffusion models Sohl-Dickstein et al. [2015], Ho et al. [2020a], are a new class of deep generative models capable of capturing complex high-dimensional distributions without requiring prior knowledge of the data’s intrinsic dimension. We show that, despite their lack of *explicit* dependence on it, these models *implicitly* estimate the data’s intrinsic dimension.

---

\*Equal contribution.

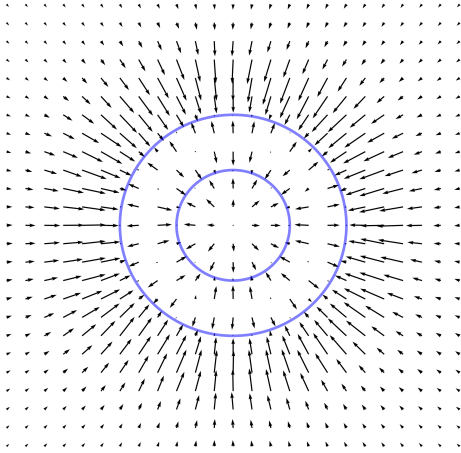


Figure 1: The data manifold (in blue) and the neural approximation of the score field  $\nabla_{\mathbf{x}} \ln p_{t_0}(\mathbf{x})$  obtained from a diffusion model. Near the manifold the score field is perpendicular to the manifold surface.

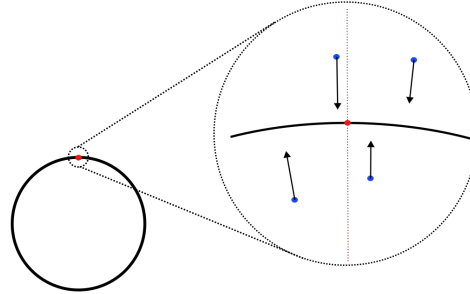


Figure 2: The red dot shows a point  $\mathbf{x}_0$  on the data manifold where we wish to estimate the dimension. We sample  $K$  blue points  $\mathbf{x}_t^{(i)}$  in a close neighbourhood of the red point and evaluate the score field. The resulting vectors  $s_{\theta}(\mathbf{x}_{\epsilon}^{(i)}, \epsilon)$  will point in the normal direction. We put the vectors into a matrix and perform SVD to detect the dimension of the normal space. The dimension of the manifold will be equal to the number of (almost) vanishing singular values.

As shown in Song et al. [2020], Ho et al. [2020a], diffusion models perform score matching Hyvärinen [2005] and, therefore, contain the information about the gradient of the log-density of the data distribution. Our approach capitalizes on the insight that near the data manifold, the gradient of the log-density is orthogonal to the manifold itself. This key observation serves as a tool for deducing the manifold’s dimension.

We evaluate the performance of the method on synthetic Euclidean and image datasets, where the dimension of the data manifold is known *a priori*. Moreover, we apply our method to the MNIST dataset LeCun and Cortes [2010] (where the intrinsic dimension is unknown), and evaluate its performance using the reconstruction error of auto-encoders trained with different latent dimensions.

## 2 Related Work

The problem of estimating the intrinsic dimensionality has been widely studied. The two main lines of research are PCA based and nearest neighbour based approaches. In an early work Fukunaga and Olsen [1971] the authors suggest an approach based on using local Karhunen–Loève expansion. In following years many PCA based approaches have been developed. Most notably, in Minka [2000] the author suggests an intrinsic dimensionality estimator based on the probabilistic PCA (PPCA) framework Bishop and Tipping [2001]. In Fan et al. [2010] a local PCA method has been suggested. In Pettis et al. [1979] authors suggested an estimator based on nearest neighbour information. In Levina and Bickel [2004] authors introduce a maximum likelihood (MLE) procedure based on the distance to  $m$  nearest neighbours. Their method has been further improved in the work of Haro et al. [2008]. The MLE method has been recently applied by Pope et al. [2021] in the estimation of the intrinsic dimensionality of modern image datasets such as MNIST LeCun and Cortes [2010], CIFAR Krizhevsky [2012] and ImageNet Deng et al. [2009]. Other works explored geometric approaches using fractal-based methods Camastra and Vinciarelli [2002] or packing numbers Kégl [2002].

To the best of our knowledge, we are the first to present a method that approximates the intrinsic dimension of the data manifold using diffusion models.

## 3 Background: Score-based diffusion models

In Song et al. [2020] score-based Hyvärinen [2005] and diffusion-based Sohl-Dickstein et al. [2015], Ho et al. [2020a] generative models were unified into a single continuous-time score-based framework where the diffusion is represented by a stochastic differential equation, which can be reversed to

generate samples. Diffusion models are trained by approximating the score function  $\nabla_{\mathbf{x}_t} \ln p_t(\mathbf{x}_t)$  with a neural network  $s_\theta(\mathbf{x}_t, t)$ . Additional details on training and sampling from diffusion models are described in Appendix A.

## 4 Proposed Method for Estimation of Intrinsic Dimension

Consider a dataset  $D = \{\mathbf{x}^{(i)}\}_{i=0}^N \sim p_0(\mathbf{x})$  which consists of  $N$  independent  $d$ -dimensional vectors  $\mathbf{x}^{(i)} \in \mathbb{R}^d$  drawn from distribution  $p_0(\mathbf{x})$ . The distribution  $p_0(\mathbf{x})$  is supported on a  $k$ -dimensional manifold  $\mathcal{M}$ , which is embedded in a space of ambient dimension  $d$ . Our goal is to infer the dimension  $k$  of the manifold  $\mathcal{M}$  from  $D$ .

We perturb the data according to the variance exploding SDE  $d\mathbf{x}_t = g(t)d\mathbf{w}_t$  Song et al. [2020] and train a neural network  $s_\theta(\mathbf{x}_t, t)$  to approximate the score function of the noise perturbed target distribution, i.e.  $\nabla_{\mathbf{x}_t} \ln p_t(\mathbf{x}_t)$  for a range of levels of perturbation indexed by diffusion time  $t$ . We train the model using the weighted denoising score matching objective with likelihood weighting, see Song et al. [2021]. More details about the training of the diffusion model can be found in Appendix B.

Consider a datapoint  $\mathbf{x}_0$  on a manifold  $\mathcal{M}$  and perturb it into the ambient space with the transition kernel  $p_{t_0}(\mathbf{x}_{t_0}|\mathbf{x}_0) = \mathcal{N}(\mathbf{x}_{t_0}|\mathbf{x}_0, \sigma_{t_0}^2 \mathbf{I})^2$  of the forward process for a small time  $t_0$ . As shown in the next section, at  $\mathbf{x}_{t_0}$  the score vector  $s_\theta(\mathbf{x}_{t_0}, t_0)$  will point towards its orthogonal projection onto  $\mathcal{M}$ , making it almost orthogonal to  $T_{\mathbf{x}_0}\mathcal{M}$  (the tangent space at  $\mathbf{x}_0$ ). This score vector will be almost entirely contained in  $\mathcal{N}_{\mathbf{x}_0}\mathcal{M}$  (the normal space at  $\mathbf{x}_0$ ) as a consequence of this, and so the rank of a matrix containing score vectors evaluated at  $K$  points diffused from  $\mathbf{x}_0$  should not exceed the dimension of  $\mathcal{N}_{\mathbf{x}_0}\mathcal{M}$ . With enough samples, the rank of  $S = [s_\theta(\mathbf{x}_{t_0}^{(1)}, t_0), \dots, s_\theta(\mathbf{x}_{t_0}^{(K)}, t_0)]$  estimates the normal space dimension, from which the manifold dimension can be estimated. In our method, we sample  $K = 4d$  diffused points at time  $t_0 = \epsilon$  and calculate the SVD of  $S$ , finally we estimate the intrinsic dimension  $\hat{k}(\mathbf{x}_0)$  as the number of vanishing singular values.

The resulting spectrum shows a significant drop exactly or very close to the dimension of the normal space. The remaining non-zero but much smaller singular values correspond to the tangential component of the score vector. This behaviour is expected as the score vector will unavoidably have a very small tangential component, for reasons explained in the following sections. The choice of the cut-off point  $\hat{k}(\mathbf{x}_0)$  is usually very clear visually, but can be automated by choosing the point of largest drop in the spectrum:

$$\hat{k}(\mathbf{x}_0) = d - \arg \max_{i=1, \dots, d-1} s_i - s_{i+1}$$

When selecting  $\mathbf{x}_0$ , we ideally want a point with high score approximation quality, minimal tangential component, and low manifold curvature. However, since these factors are uncontrollable, we randomly choose multiple  $\mathbf{x}_0^{(j)}$  values and plot a spectrum for each. For simple distributions, the score spectra look similar, with drops at accurate values. For more complex distributions, the drop location varies with  $\mathbf{x}_0^{(j)}$  choice. We find that the maximum estimated  $\hat{k}$  gives the best estimate. Theoretical understanding of the method supports this, as discussed in later sections.

<sup>2</sup>The transition kernels of the variance exploding SDE have this structure, where  $\sigma_t$  is an increasing function determined by  $g(t)$  with  $\sigma_t \xrightarrow{t \rightarrow 0} 0$ .

---

**Algorithm 1:** Estimate the intrinsic dimension at  $\mathbf{x}_0$

---

**Input:**  $s_\theta$  - trained diffusion model (score),  
 $t_0$  - sampling time,  
 $K$  - number of score vectors.

Sample  $\mathbf{x}_0 \sim p_0(\mathbf{x})$  from the data set

$d \leftarrow \dim(\mathbf{x}_0)$

$S \leftarrow$  empty matrix

**for**  $i = 1, \dots, K$  **do**

    Sample  $\mathbf{x}_{t_0}^{(i)} \sim \mathcal{N}(\mathbf{x}_{t_0}|\mathbf{x}_0, \sigma_{t_0}^2 \mathbf{I})$

    Append  $s_\theta(\mathbf{x}_{t_0}^{(i)}, t_0)$  as a new column to  $S$

**end**

$(s_i)_{i=1}^d, (\mathbf{v}_i)_{i=1}^d, (\mathbf{w}_i)_{i=1}^d \leftarrow \text{SVD}(S)$

$\hat{k}(\mathbf{x}_0) \leftarrow d - \arg \max_{i=1, \dots, d-1} (s_i - s_{i+1})$

**Output:**  $\hat{k}(\mathbf{x}_0)$

---

where  $(s_i)_{i=1}^d, (v_i)_{i=1}^d, (w_i)_{i=1}^d$  denote singular values, left and right singular vectors respectively.

## 5 Theoretical Analysis

Here we provide a theoretical justification of our approach; showing that given a collection of points  $\mathbf{x}_i \in \mathbb{R}^d$  sufficiently close<sup>3</sup> to the manifold with orthogonal projection  $\pi(\mathbf{x}_i) \in \mathcal{M}$ , in the small  $t$  limit the space spanned by score vectors  $\nabla_{\mathbf{x}} \ln p_t(\mathbf{x}_i)$  converges to the normal space at  $\pi(\mathbf{x}_i)$ . To build intuition, consider a uniform data density on the manifold surface  $\mathcal{M}$ . The gradient along this density is zero, indicating that for  $\mathbf{x}$  close to  $\mathcal{M}$  tangential components of the score  $\nabla_{\mathbf{x}} \ln p_t(\mathbf{x})$  will also be approximately zero and the score will be mostly contained in the normal bundle  $\mathcal{NM}$ . If the density is non-uniform on the manifold surface however, the score will have a tangential component. Fortunately, for sufficiently small  $t$  the change in log-density from moving orthogonally towards the manifold dominates the change from moving tangentially alongside the manifold. This results in the tangential component becoming negligible, and the score still being approximately contained in  $\mathcal{NM}$ .

Specifically, we show in the following theorem that for any point  $\mathbf{x}$  sufficiently close to the data manifold and  $t \rightarrow 0$ , the score  $\nabla_{\mathbf{x}} \ln p_t(\mathbf{x})$  points directly at the orthogonal projection  $\pi(\mathbf{x})$ .

**Theorem 5.1.** *Suppose that the support of the data distribution  $P_0$  is contained in a compact embedded sub-manifold  $\mathcal{M} \subseteq \mathbb{R}^d$  and let  $P_t$  be the distribution of samples from  $P_0$  diffused for time  $t$ . Then, under mild assumptions, for any point  $\mathbf{x} \in \mathbb{R}^d$  sufficiently close to  $\mathcal{M}$  with orthogonal projection on  $\mathcal{M}$ , given by  $\pi(\mathbf{x})$ , and  $\mathbf{n} = (\pi(\mathbf{x}) - \mathbf{x}) / \|\pi(\mathbf{x}) - \mathbf{x}\|$ , we have:*

$$S_{\cos}(\mathbf{n}, \nabla_{\mathbf{x}} \ln p_t(\mathbf{x})) \xrightarrow[t \rightarrow 0]{} 1$$

where  $S_{\cos}$  denotes the cosine similarity. In other words, for sufficiently small  $t$  the score  $\nabla_{\mathbf{x}} \ln p_t(\mathbf{x})$  points directly at the projection of  $\mathbf{x}$  on the manifold.

This theorem leads to the conclusion that this score is contained within the normal space of the manifold, as we show with the following corollary:

**Corollary 5.2.** *The ratio of the projection of the score  $\nabla_{\mathbf{x}} \ln p_t(\mathbf{x})$  on the tangent space of the data manifold  $T_{\pi(\mathbf{x})}\mathcal{M}$  to the projection on the normal space  $\mathcal{N}_{\pi(\mathbf{x})}\mathcal{M}$  approaches zero as  $t$  approaches zero, i.e.*

$$\frac{\|\mathbf{T}\nabla_{\mathbf{x}} \ln p_t(\mathbf{x})\|}{\|\mathbf{N}\nabla_{\mathbf{x}} \ln p_t(\mathbf{x})\|} \rightarrow 0, \text{ as } t \rightarrow 0.$$

where  $\mathbf{N}$  and  $\mathbf{T}$  are projection matrices on  $\mathcal{N}_{\pi(\mathbf{x})}\mathcal{M}$  and  $T_{\pi(\mathbf{x})}\mathcal{M}$  respectively. Therefore for sufficiently small  $t$  the score  $\nabla_{\mathbf{x}} \ln p_t(\mathbf{x})$  is (effectively) contained in the normal space  $\mathcal{N}_{\pi(\mathbf{x})}\mathcal{M}$ .

*Proof.* The full proof of the theorem and corollary can be found in the Appendix D.

In practice we choose small  $t > 0$ , and for each chosen  $\mathbf{x}_0 \in \mathcal{M}$  we sample points  $\mathbf{x}_t^{(i)}$  around it from  $p_t(\mathbf{x}_t|\mathbf{x}_0) = \mathcal{N}(\mathbf{x}_t|\mathbf{x}_0, \sigma_t^2\mathbf{I})$ . With over 99% probability  $\mathbf{x}_t^{(i)} \in B(\mathbf{x}_0, 3\sigma_t)$ , and so as we decrease  $t$  most of our  $\mathbf{x}_t$  will become very close to  $\mathbf{x}_0$ . For  $B(\mathbf{x}_0, 3\sigma_t)$  sufficiently small, the effect of curvature of  $\mathcal{M}$  becomes negligible inside  $B(\mathbf{x}_0, 3\sigma_t)$ , and so the normal spaces  $\mathcal{N}_{\pi(\mathbf{x}_t^{(i)})}\mathcal{M}$  will all be approximately equal to  $\mathcal{N}_{\mathbf{x}_0}\mathcal{M}$ . Under this assumption, we can outline the practical implications of these theoretical results. Assuming  $t > 0$  small and a trained score approximation  $s_{\theta}(\mathbf{x}, t) \approx \nabla_{\mathbf{x}} \ln p_t(\mathbf{x})$ , the score matrix  $S = [s_{\theta}(\mathbf{x}_t^{(1)}, t), \dots, s_{\theta}(\mathbf{x}_t^{(4d)}, t)]$  has the following properties:

1. The columns of  $S$  are approximately contained in the normal space  $\mathcal{N}_{\mathbf{x}_0}\mathcal{M}$
2. The columns of  $S$  approximately span the normal space  $\mathcal{N}_{\mathbf{x}_0}\mathcal{M}$
3. The singular values of  $S$  corresponding to singular vectors in the normal space are large relative to those corresponding to tangent singular vectors

The first point is a direct consequence of Corollary 5.2. For the second point, denote  $n_{\mathbf{x}} := \frac{\pi(\mathbf{x}) - \mathbf{x}}{\|\pi(\mathbf{x}) - \mathbf{x}\|}$ , and assume that  $t$  is sufficiently small such that  $\mathcal{N}_{\pi(\mathbf{x}_t^{(i)})}\mathcal{M} \approx \mathcal{N}_{\mathbf{x}_0}\mathcal{M}$ . Then locally, the vectors  $\{n_{\mathbf{x}_t^{(1)}}, \dots, n_{\mathbf{x}_t^{(K)}}\}$  are independent Gaussian perturbations from a linear subspace. With

<sup>3</sup>For ‘sufficiently close’ to be defined in Appendix D

probability one this set contains  $N_d = \dim(\mathcal{N}_{\mathbf{x}_0}\mathcal{M})$  linearly independent vectors spanning  $\mathcal{N}_{\mathbf{x}_0}\mathcal{M}$ , so by Theorem 5.1 the score vectors  $\{\nabla_{\mathbf{x}} \ln p_t(\mathbf{x}_t^{(1)}), \dots, \nabla_{\mathbf{x}} \ln p_t(\mathbf{x}_t^{(K)})\}$  must therefore also span  $\mathcal{N}_{\mathbf{x}_0}\mathcal{M}$ . For the third point note that if the columns of  $S$  span  $\mathcal{N}_{\mathbf{x}_0}\mathcal{M}$ , then  $S$  has rank  $N_d$ , and its SVD yields singular values  $s_i > 0$  for  $i \leq N_d$  corresponding to singular vectors in  $\mathcal{N}_{\mathbf{x}_0}\mathcal{M}$ , and  $s_j = 0$  for  $j > N_d$ . In practice we fix some small  $t > 0$  and so small components of  $T_{\mathbf{x}_0}\mathcal{M}$  are introduced to the score by factors such as non-uniform distribution of data samples on  $\mathcal{M}$ , therefore in applications the SVD of  $S$  yields small singular values  $s_j > 0$  for  $j > N_d$ , however we still observe that  $s_i \gg s_j$  where  $i \leq N_d$ .

## 6 Limitations

In section 5, we established that given a perfect score approximation for sufficiently low  $t$  our method produces the correct estimation of the dimension. However, in practice, our method may encounter two types of errors: *approximation error* and *geometric error*. The approximation error arises as a result of having an imperfect score approximation  $s_\theta(\mathbf{x}, t) \approx \nabla_{\mathbf{x}} \ln p_t(\mathbf{x})$ . Geometric error arises if the selected sampling time  $t$  isn't sufficiently small, potentially impacting our method's accuracy for two reasons. Firstly, it may result in an increased tangential component of the score vector. Secondly, if  $\mathbf{x}_t^{(i)}$  lies too distant from  $\mathcal{M}$ , the manifold's curvature may create a difference between normal spaces  $\mathcal{N}_{\pi(\mathbf{x}_t^{(i)})}\mathcal{M}$  across varying  $i$ .

We empirically assess our method's robustness to approximation error and find it robust to minor inaccuracies in score approximation. Additionally, we analyze our method's sensitivity to  $p_0$  non-uniformity, which could induce a minor tangential score component for  $t > 0$ . We discover that using the maximum  $\hat{k}(\mathbf{x}_0^{(j)})$  allows our method to accommodate varying levels of non-uniformity over the manifold surface, displaying superior robustness compared to other non-linear estimators (MLE, Local PCA) without the need for reducing  $t$ . Details are in Appendix G

We note that Theorem 5.1 assumes the data distribution's support is exclusively within a manifold. Therefore, we empirically investigate the method's applicability when data is concentrated around, but not entirely within, a manifold. We discover that for a  $k$ -sphere, our method remains reliable as long as the data is closely concentrated around the manifold. Details are available in Appendix G.

## 7 Experiments

We examine the effectiveness of our method on a multitude of manifold datasets, each embedded in a high-dimensional ambient space. The datasets fall into two categories: *Euclidean datasets* consisting of points from manifolds embedded in a high-dimensional Euclidean space and *image datasets* consisting of synthetic manifolds of images. In each case we know the intrinsic dimension of the manifold *a priori*. Additionally, we apply our method to the MNIST dataset, where the true intrinsic dimension is unknown. We assess its performance via comparison with the reconstruction error of auto-encoders with various latent dimensions. For each dataset we train a diffusion model, and then apply our method to estimate the intrinsic dimension of the data manifold. Details on hyperparameters and architectures used in our experiments can be found in Appendix B.

We compare our method against established approaches to intrinsic dimensionality estimation: the nearest neighbour based maximum likelihood estimator (MLE) Levina and Bickel [2004], Haro et al. [2008], Local PCA Fan et al. [2010] and Probabilistic PCA (PPCA) Minka [2000] Bishop and Tipping [2001]. The details about the implementation of the benchmarks are in the Appendix C.

Our method consistently yields the best estimate or close to the best estimate among considered approaches. In the following subsections we present a detailed discussion of each experiment. The results are summarised in Table 2.

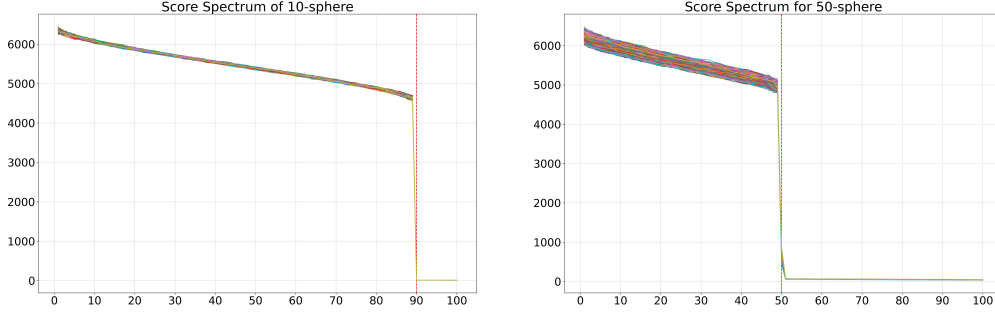


Figure 3: Singular values for the scores of  $k$ -sphere for  $k = 10, 50$ . In both cases around  $k$  singular values almost vanish, clearly indicating the dimensionality of the manifold. Each line shows a score spectrum at different  $\mathbf{x}_0^{(j)}$ .

## 7.1 Experiments on Euclidean datasets

**Embedded  $k$ -spheres:** We examined our method on  $k$  dimensional spheres embedded in a  $d = 100$  dimensional ambient space via a random isometric embedding<sup>4</sup>. We consider two cases  $k_1 = 10$  and  $k_2 = 50$ . The spectra of resulting score matrices are presented in Figure 3. Our method gives estimates of  $\hat{k}_1 = 11$  and  $\hat{k}_2 = 51$ , which are very close to the true intrinsic dimensionality of the manifolds.

**Spaghetti line:** The intrinsic dimensionality of  $k$ -spheres could be well approximated by a linear dimensionality detection methods such as Minka [2000]. This is because these manifolds are contained in a low dimensional *linear* subspace. In order to showcase the advantage of the *non-linear* nature of our method we consider a *spaghetti line* manifold. That is a curve  $t \mapsto (\sin(t), \sin(2t), \dots, \sin(100t))$  in a 100 dimensional ambient space, which is not contained in any low dimensional linear subspace (cf. Figure 9 in Appendix F.1). As expected, the linear method Minka [2000] greatly overstates the intrinsic dimension with a result of  $\hat{k}_{\text{PPCA}} = 98$ . Yet, our approach utilizes the non-linear knowledge from the diffusion model to accurately predict an intrinsic dimensionality of one. The score spectrum is presented in Figure 10 in Appendix F.1.

**Union of  $k$ -spheres:** Due to the local nature of our method, we are able to generate an estimate  $\hat{k}(\mathbf{x}_0)$  of the intrinsic dimension around a given point  $\mathbf{x}_0$ . This allows us to apply our approach to a union of manifolds and identify the dimension of each component. We illustrate this feature with the following experiment. We embed two spheres of different radii and dimensions in a 100 dimensional ambient space. First sphere has dimension  $k_1 = 10$  and radius  $r_1 = 1$  and the second sphere has  $k_2 = 30$  and radius  $r_2 = 0.25$ <sup>5</sup>. We apply our method to this data using multiple  $\mathbf{x}_0^{(i)}$  randomly sampled from the dataset. We observe that our method produces a spectrum with two visible, separated drops. This indicates that the data comes from the union of manifolds of different dimensions. The resulting estimates are  $\hat{k}_1 = 10$  and  $\hat{k}_2 = 31$  depending on the chosen  $\mathbf{x}_0^{(j)}$ . The score spectra and the histogram of estimated dimensions are presented in Figures 11 and 12 in Appendix F.1.

## 7.2 Experiments on image datasets

**Synthetic image manifolds:** In this experiment, we investigated our method’s ability to infer the dimension of synthetic image manifolds with known dimension. We crafted two synthetic image manifolds with controllable intrinsic dimension  $k$ : the " $k$  squares images manifold" and the " $k$  Gaussian blobs images manifold". The construction of these manifolds is detailed in Appendix E. We evaluated our method on  $k = 10, 20$ , and 100 dimensional manifolds for both types, with the score

<sup>4</sup>To obtain a random isometric embedding we first generate the  $k$  sphere in a  $k + 1$  dimensional small ambient space. Then we sample a random  $d \times (k + 1)$  Gaussian matrix  $A$ . We perform a QR decomposition  $A = QR$ . Finally we use the  $d \times (k + 1)$  isometry matrix  $Q$  to embed the small  $k + 1$  dimensional space containing our manifold in the large  $d$  dimensional ambient space.

<sup>5</sup>One can intuitively think of this manifold as a high-dimensional analog of a planet with a ring around it.

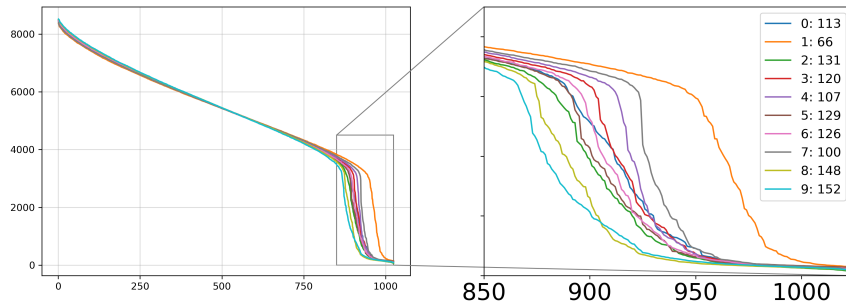


Figure 5: MNIST score spectra that yielded the highest estimated dimension for each digit

spectra and histograms of estimated dimensions for numerous data points displayed in Figures 13 and 14 in Appendix F.2.

On the squares image manifold, only our method and PPCA consistently yielded accurate dimension estimates. PPCA’s success on this dataset was anticipated since the manifold resides within a  $k$ -dimensional linear subspace.

On the Gaussian blobs image manifold, our method stood out as the sole technique to consistently deliver accurate dimension estimates. The accuracy of our method was not compromised by the manifold’s increased complexity, unlike other methods. However, the estimation for the 100-dimensional manifold introduced some uncertainty, as indicated by a more leveled histogram and a less abrupt spectrum collapse (c.f. Figure 14). This is attributed to the manifold’s increased complexity and the inherent challenges in optimization, resulting in greater geometrical and statistical errors.

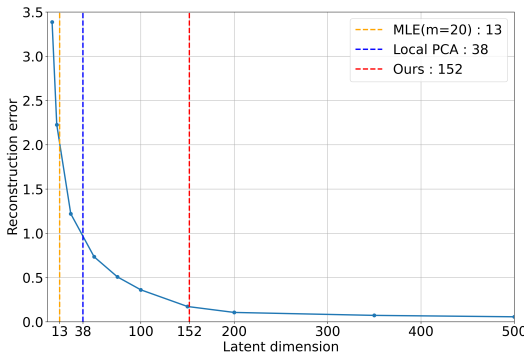


Figure 4: Auto-encoder reconstruction error on MNIST for different latent space dimensions. Vertical lines mark different estimations of intrinsic dimension.

**MNIST:** In our study, we additionally applied the proposed technique to estimate the intrinsic dimension of the well-known MNIST dataset - an image dataset with an as-of-yet-undetermined intrinsic dimension. Our findings suggest that there exists a variation in the intrinsic dimensions across different digits. For instance, the digit ‘1’ yielded an estimated dimension of 66, whereas the digit ‘9’ exhibited a significantly higher estimated dimension of 152. This discrepancy can be attributed to the increased geometric complexity inherent to the digit ‘9’. Figure 5 elucidates these observations by displaying the score spectra which yielded the maximum estimated dimensions for each digit. We present the estimated dimension for each digit in Table 1 and the complete set of spectra for each digit in the Appendix F.3.

We validate our estimates by comparing them with the reconstruction error of auto-encoders trained with different latent dimensions. As shown in Figure 4 the intrinsic dimension obtained with our method coincides with the point of diminishing returns in terms of reduction of the reconstruction loss. Contrastingly, estimates produced by MLE and Local PCA were significantly lower, corresponding to regions of the curve where the reconstruction loss was still steeply decreasing. This suggests these methods underestimate the true manifold dimension. These findings call for a careful interpretation of the intrinsic dimension estimates of popular machine learning datasets provided by Pope et al. [2021], as they rely on the MLE method, which we have found to consistently underestimate manifold dimensions. On the other hand, PPCA notably overestimated the dimension, with  $\hat{k}_{\text{PPCA}} = 706$ .

0	1	2	3	4	5	6	7	8	9
113	66	131	120	107	129	126	100	148	152

Table 1: Estimated intrinsic dimension for each MNIST digit

	Ground Truth	Ours	MLE (m=5)	MLE (m=20)	Local PCA	PPCA
Euclidean Data Manifolds						
10-sphere	10	11	9.61	9.46	11	11
50-sphere	50	51	35.52	34.04	51	51
Spaghetti line	1	1	1.01	1.00	32	98
Image Manifolds						
Squares						
$k = 10$	10	11	8.48	8.17	10	10
$k = 20$	20	22	14.96	14.36	20	20
$k = 100$	100	100	37.69	34.42	78	99
Gaussian blobs						
$k = 10$	10	12	8.88	8.67	10	136
$k = 20$	20	21	16.34	15.75	20	264
$k = 100$	100	98	39.66	35.31	18	985
MNIST	N/A	152	14.12	13.27	38	706

Table 2: Comparison of dimensionality detection methods on various data manifolds.

## 8 Conclusions and further directions

In this work, we proved theoretically and confirmed experimentally that diffusion models can infer the intrinsic dimension from the data. We introduced an approach that estimates the intrinsic dimension of the data manifold from a pre-trained diffusion model. This approach capitalizes on the observation that, the diffusion model evaluated at sufficiently small diffusion time approximates the normal bundle of the data manifold. Our work offers a twofold contribution: it highlights that diffusion model detects the lower dimensional structure of data and provides a rigorous method for intrinsic dimension estimation.

Our method has been rigorously tested on Euclidean and image data and has consistently provided accurate estimates of the intrinsic dimension, outperforming established statistical estimators, especially in higher dimensional manifolds. Furthermore, our research introduces new estimates for the MNIST’s dimensionality, demonstrating strong alignment with the predictions of an auto-encoder trained across a range of latent dimensions.

We are the first, to our knowledge, to present an intrinsic dimension estimation method based on diffusion models. The superior performance of our approach on higher dimensional manifolds compared to statistical estimators is attributed to the enhanced statistical efficiency from the inductive biases in the neural network architectures approximating the score function. Our work opens new paths for understanding and estimating intrinsic data dimension, with potential implications across the field of machine learning. Future research should explore this method’s applicability to other data types and its potential across various domains.

## References

- Brian D.O. Anderson. Reverse-time diffusion equation models. *Stochastic Processes and their Applications*, 12(3):313–326, 1982. ISSN 0304-4149. doi: [https://doi.org/10.1016/0304-4149\(82\)90051-5](https://doi.org/10.1016/0304-4149(82)90051-5). URL <https://www.sciencedirect.com/science/article/pii/0304414982900515>.
- C M Bishop and M E Tipping. Probabilistic principal component analysis. 2001. PPCA.
- F. Camastra and A. Vinciarelli. Estimating the intrinsic dimension of data with a fractal-based method. *IEEE Transactions on Pattern Analysis and Machine Intelligence*, 24(10):1404–1407, 2002. doi:

- 10.1109/TPAMI.2002.1039212.
- Jia Deng, Wei Dong, Richard Socher, Li-Jia Li, Kai Li, and Li Fei-Fei. Imagenet: A large-scale hierarchical image database. In *2009 IEEE Conference on Computer Vision and Pattern Recognition*, pages 248–255, 2009. doi: 10.1109/CVPR.2009.5206848.
- Mingyu Fan, Nannan Gu, Hong Qiao, and Bo Zhang. Intrinsic dimension estimation of data by principal component analysis, 2010. URL <https://arxiv.org/abs/1002.2050>.
- Charles Fefferman, Sanjoy Mitter, and Hariharan Narayanan. Testing the manifold hypothesis, 2013. URL <https://arxiv.org/abs/1310.0425>.
- K. Fukunaga and D.R. Olsen. An algorithm for finding intrinsic dimensionality of data. *IEEE Transactions on Computers*, C-20(2):176–183, 1971. doi: 10.1109/T-C.1971.223208.
- Ian J. Goodfellow, Jean Pouget-Abadie, Mehdi Mirza, Bing Xu, David Warde-Farley, Sherjil Ozair, Aaron Courville, and Yoshua Bengio. Generative adversarial networks, 2014. URL <https://arxiv.org/abs/1406.2661>.
- Gloria Haro, Gregory Randall, and Guillermo Sapiro. Translated poisson mixture model for stratification learning. *Int. J. Comput. Vis.*, 80(3):358–374, 2008.
- Geoffrey E Hinton and Sam Roweis. Stochastic neighbor embedding. In S. Becker, S. Thrun, and K. Obermayer, editors, *Advances in Neural Information Processing Systems*, volume 15. MIT Press, 2002. URL <https://proceedings.neurips.cc/paper/2002/file/6150ccc6069bea6b5716254057a194ef-Paper.pdf>.
- Jonathan Ho, Ajay Jain, and Pieter Abbeel. Denoising diffusion probabilistic models, 2020a. URL <https://arxiv.org/abs/2006.11239>.
- Jonathan Ho, Ajay Jain, and Pieter Abbeel. Denoising diffusion probabilistic models. *Advances in Neural Information Processing Systems*, 33:6840–6851, 2020b.
- Aapo Hyvärinen. Estimation of non-normalized statistical models by score matching. *Journal of Machine Learning Research*, 6(24):695–709, 2005. URL <http://jmlr.org/papers/v6/hyvarinen05a.html>.
- Kerstin Johansson. intrinsicdimension: Intrinsic dimension estimation, 2016. URL <https://cran.r-project.org/web/packages/intrinsicDimension/>.
- Balázs Kégl. Intrinsic dimension estimation using packing numbers. In S. Becker, S. Thrun, and K. Obermayer, editors, *Advances in Neural Information Processing Systems*, volume 15. MIT Press, 2002. URL <https://proceedings.neurips.cc/paper/2002/file/1177967c7957072da3dc1db4ceb30e7a-Paper.pdf>.
- Diederik P Kingma and Max Welling. Auto-encoding variational bayes, 2013. URL <https://arxiv.org/abs/1312.6114>.
- Alex Krizhevsky. Learning multiple layers of features from tiny images. *University of Toronto*, 05 2012.
- Yann LeCun and Corinna Cortes. MNIST handwritten digit database. 2010. URL <http://yann.lecun.com/exdb/mnist/>.
- J.M. Lee. *Introduction to Riemannian Manifolds*. Graduate Texts in Mathematics. Springer International Publishing, 2019. ISBN 9783319917542. URL <https://books.google.co.uk/books?id=UIPltQEACAAJ>.
- Elizaveta Levina and Peter Bickel. Maximum likelihood estimation of intrinsic dimension. In L. Saul, Y. Weiss, and L. Bottou, editors, *Advances in Neural Information Processing Systems*, volume 17. MIT Press, 2004. URL <https://proceedings.neurips.cc/paper/2004/file/74934548253bcab8490ebd74afed7031-Paper.pdf>.

- Thomas Minka. Automatic choice of dimensionality for pca. In T. Leen, T. Dietterich, and V. Tresp, editors, *Advances in Neural Information Processing Systems*, volume 13. MIT Press, 2000. URL <https://proceedings.neurips.cc/paper/2000/file/7503cfacd12053d309b6bed5c89de212-Paper.pdf>.
- L. Nicolaescu. *An Invitation to Morse Theory*. Universitext. Springer New York, 2011. ISBN 9781461411055. URL <https://books.google.co.uk/books?id=nCgvt2MY4QAC>.
- R.S. Palais and C. Terng. *Critical Point Theory and Submanifold Geometry*. Critical Point Theory and Submanifold Geometry. Richard S. Palais, 1988. ISBN 9783540503996. URL <https://books.google.co.uk/books?id=ViSHzQEACAAJ>.
- Karl Pearson. LIII. On lines and planes of closest fit to systems of points in space, November 1901. URL <https://doi.org/10.1080/14786440109462720>.
- Fabian Pedregosa, Gaël Varoquaux, Alexandre Gramfort, Vincent Michel, Bertrand Thirion, Olivier Grisel, Mathieu Blondel, Peter Prettenhofer, Ron Weiss, Vincent Dubourg, et al. Scikit-learn: Machine learning in python. *Journal of machine learning research*, 12(Oct):2825–2830, 2011.
- Karl W. Pettis, Thomas A. Bailey, Anil K. Jain, and Richard C. Dubes. An intrinsic dimensionality estimator from near-neighbor information. *IEEE Transactions on Pattern Analysis and Machine Intelligence*, PAMI-1(1):25–37, 1979. doi: 10.1109/TPAMI.1979.4766873.
- Phillip Pope, Chen Zhu, Ahmed Abdelkader, Micah Goldblum, and Tom Goldstein. The intrinsic dimension of images and its impact on learning. *arXiv preprint arXiv:2104.08894*, 2021.
- Jascha Sohl-Dickstein, Eric A. Weiss, Niru Maheswaranathan, and Surya Ganguli. Deep unsupervised learning using nonequilibrium thermodynamics, 2015. URL <https://arxiv.org/abs/1503.03585>.
- Yang Song, Jascha Sohl-Dickstein, Diederik P Kingma, Abhishek Kumar, Stefano Ermon, and Ben Poole. Score-based generative modeling through stochastic differential equations. *arXiv preprint arXiv:2011.13456*, 2020.
- Yang Song, Conor Durkan, Iain Murray, and Stefano Ermon. Maximum likelihood training of score-based diffusion models. *Advances in Neural Information Processing Systems*, 34:1415–1428, 2021.
- Pascal Vincent. A connection between score matching and denoising autoencoders. *Neural Computation*, 23(7):1661–1674, 2011. doi: 10.1162/NECO\_a\_00142.

## A Extended background on diffusion models

**Setup:** In Song et al. [2020] score-based Hyvärinen [2005] and diffusion-based Sohl-Dickstein et al. [2015], Ho et al. [2020a] generative models have been unified into a single continuous-time score-based framework where the diffusion is driven by a stochastic differential equation. This framework relies on Anderson’s Theorem Anderson [1982], which states that under certain Lipschitz conditions on the drift coefficient  $f : \mathbb{R}^{n_x} \times \mathbb{R} \rightarrow \mathbb{R}^{n_x}$  and on the diffusion coefficient  $G : \mathbb{R}^{n_x} \times \mathbb{R} \rightarrow \mathbb{R}^{n_x} \times \mathbb{R}^{n_x}$  and an integrability condition on the target distribution  $p_0(\mathbf{x}_0)$  a forward diffusion process governed by the following SDE:

$$d\mathbf{x}_t = f(\mathbf{x}_t, t)dt + G(\mathbf{x}_t, t)d\mathbf{w}_t \quad (1)$$

has a reverse diffusion process governed by the following SDE:

$$d\mathbf{x}_t = [f(\mathbf{x}_t, t) - G(\mathbf{x}_t, t)G(\mathbf{x}_t, t)^T \nabla_{\mathbf{x}_t} \ln p_t(\mathbf{x}_t)]dt + G(\mathbf{x}_t, t)d\bar{\mathbf{w}}_t, \quad (2)$$

where  $\bar{\mathbf{w}}_t$  is a standard Wiener process in reverse time.

The forward diffusion process transforms the *target distribution*  $p_0(\mathbf{x}_0)$  to a *diffused distribution*  $p_T(\mathbf{x}_T)$  after diffusion time  $T$ . By appropriately selecting the drift and the diffusion coefficients of the forward SDE, we can make sure that after sufficiently long time  $T$ , the diffused distribution  $p_T(\mathbf{x}_T)$  approximates a simple distribution, such as  $\mathcal{N}(\mathbf{0}, \mathbf{I})$ . We refer to this simple distribution as the *prior distribution*, denoted by  $\pi$ . The reverse diffusion process transforms the diffused distribution  $p_T(\mathbf{x}_T)$  to the data distribution  $p_0(\mathbf{x}_0)$  and the prior distribution  $\pi$  to a distribution  $p^{SDE}$ . The distribution  $p^{SDE}$  is close to  $p_0(\mathbf{x}_0)$  if the diffused distribution  $p_T(\mathbf{x}_T)$  is close to the prior distribution  $\pi$ . We get samples from  $p^{SDE}$  by sampling from  $\pi$  and simulating the reverse SDE from time  $T$  to time 0.

**Sampling:** To get samples by simulating the reverse SDE, we need access to the time-dependent score function  $\nabla_{\mathbf{x}_t} \ln p_t(\mathbf{x}_t)$ . In practice, we approximate the time-dependent score function with a neural network  $s_\theta(\mathbf{x}_t, t) \approx \nabla_{\mathbf{x}_t} \ln p_t(\mathbf{x}_t)$  and simulate the reverse SDE presented in equation 3 to map the prior distribution  $\pi$  to  $p_\theta^{SDE}$ .

$$d\mathbf{x}_t = [f(\mathbf{x}_t, t) - G(\mathbf{x}_t, t)G(\mathbf{x}_t, t)^T s_\theta(\mathbf{x}_t, t)]dt + G(\mathbf{x}_t, t)d\bar{\mathbf{w}}_t, \quad (3)$$

If the prior distribution is close to the diffused distribution and the approximated score function is close to the ground truth score function, the modeled distribution  $p_\theta^{SDE}$  is provably close to the target distribution  $p_0(\mathbf{x}_0)$ . This statement is formalised in the language of distributional distances in the work of Song et al. [2021].

**Training:** A neural network  $s_\theta(\mathbf{x}_t, t)$  can be trained to approximate the score function  $\nabla_{\mathbf{x}_t} \ln p_t(\mathbf{x}_t)$  by minimizing the weighted score matching objective

$$\mathcal{L}_{SM}(\theta, \lambda(\cdot)) := \frac{1}{2} \mathbb{E}_{\substack{t \sim U(0, T) \\ \mathbf{x}_t \sim p_t(\mathbf{x}_t)}} [\lambda(t) \|\nabla_{\mathbf{x}_t} \ln p_t(\mathbf{x}_t) - s_\theta(\mathbf{x}_t, t)\|_2^2] \quad (4)$$

where  $\lambda : [0, T] \rightarrow \mathbb{R}_+$  is a positive weighting function.

However, the above quantity cannot be optimized directly since we don’t have access to the ground truth score  $\nabla_{\mathbf{x}_t} \ln p_t(\mathbf{x}_t)$ . Therefore in practice, a different objective has to be used Hyvärinen [2005], Vincent [2011], Song et al. [2020]. In Song et al. [2020], the weighted denoising score-matching objective is used, which is defined as

$$\mathcal{L}_{DSM}(\theta, \lambda(\cdot)) := \frac{1}{2} \mathbb{E}_{\substack{t \sim U(0, T) \\ \mathbf{x}_0 \sim p_0(\mathbf{x}_0) \\ \mathbf{x}_t \sim p_t(\mathbf{x}_t | \mathbf{x}_0)}} [\lambda(t) \|\nabla_{\mathbf{x}_t} \ln p_t(\mathbf{x}_t | \mathbf{x}_0) - s_\theta(\mathbf{x}_t, t)\|_2^2] \quad (5)$$

The difference between DSM and SM is the replacement of the ground truth score which we do not know by the score of the perturbation kernel which we know analytically for many choices of forward SDEs. The choice of the weighted DSM objective is justified because the weighted DSM objective is equal to the SM objective up to a constant that does not depend on the parameters of the model  $\theta$ . The reader can refer to Vincent [2011] for the proof.

## B Training details

We trained the score model using the weighted denoising score matching objective Song et al. [2020], presented in eq. 6. We used the likelihood weighting function, i.e.  $\lambda(t) = g(t)^2$ , where  $g(t)$  is the diffusion coefficient of the forward SDE.

$$\mathcal{L}_{DSM}(\theta, \lambda(\cdot)) := \frac{1}{2} \mathbb{E}_{t \sim U(0, T)} \mathbb{E}_{\mathbf{x}_0 \sim p_0(\mathbf{x}_0)} \mathbb{E}_{\mathbf{x}_t \sim p_t(\mathbf{x}_t | \mathbf{x}_0)} [\lambda(t) \|\nabla_{\mathbf{x}_t} \ln p_t(\mathbf{x}_t | \mathbf{x}_0) - s_\theta(\mathbf{x}_t, t)\|_2^2] \quad (6)$$

### B.1 Euclidean data

For all of our experiments on Euclidean data, we used a fully connected network with 5 hidden layers and 2048 nodes in each hidden layer to approximate the score function. The input and output dimension is the same as the ambient dimension. For the optimisation of the model, we used the Adam algorithm with a learning rate of  $2e-5$  and exponential moving average (EMA) on the weights of the model with a decay rate of 0.9999. Moreover, we chose the variance exploding SDE Song et al. [2020] as the forward process with  $\sigma_{min} = 0.01$  and  $\sigma_{max} = 4$ .

### B.2 Image data

For all our of our experiments on image data, we used the DDPM architecture Ho et al. [2020b] with variance exploding SDE Song et al. [2020] and hyperparameters indicated in Table 3.

### B.3 Auto-encoder

The encoder and decoder encoder architectures are based on the DDPM U-Net Ho et al. [2020a], which we call half-U nets.

For the encoder we used the downsampling part of the U-Net and removed the upsampling part and the skip connections. The downscaled tensor is flattened and mapped to the latent dimension with an additional linear layer.

For the decoder we start by linearly transforming the latent vector and reshaping it into a tensor of appropriate dimension. Then we used the upsampling part of the DDPM U-Net.

We used the Adam optimizer and EMA rate 0.999. We used learning rate scheduler reducing the loss on plateau starting form  $10^{-4}$  and stopping at  $10^{-5}$ . We trained the auto-encoder for each latent dimension for 36h on NVIDIA A-100 GPU. At the end we used checkpoints which minimized the validation loss to evaluate the reconstruction error.

All other hyperparameters are included in Table 3.

Hyper-parameter	MNIST	Synthetic Image data
Number of filters	128	128
Channel multipliers	(1, 2, 2, 4)	(1, 2, 2, 2)
Dropout	0.1	0.1
EMA rate	0.999	0.999
Normalization	GroupNorm	GroupNorm
Nonlinearity	Swish	Swish
Number of residual blocks	4	4
Attention resolution	16	16
Convolution size	3	3
$\sigma_{min}$	0.009	0.01
$\sigma_{max}$	50	50
Learning rate	Scheduler( $10^{-4}, 10^{-5}$ )	$2 \cdot 10^{-4}$

Table 3: DDPM Model Parameters

## C Benchmarking

We compared our method against well established approaches to intrinsic dimensionality estimation: the MLE estimator Levina and Bickel [2004], Haro et al. [2008], Local PCA Fan et al. [2010] and Probabilistic PCA Minka [2000] Bishop and Tipping [2001]. For MLE estimator and local PCA we used the implementation provided in the R package INTRINSICDIMENSION Johnsson [2016]. The MLE estimator has an important hyperparameter  $m$  - the number of nearest neighbour distances that should be used for the dimension estimation. We used values  $m = 5$  and  $20$  since these are extremal values considered in Pope et al. [2021]. For PPCA we used the SCIKIT-LEARN implementation Pedregosa et al. [2011]. The code for reproducing the benchmarking experiments is included in our codebase.

## D Proofs

Here we provide full proofs for the statements in Section 5. First, we show that for any point  $\mathbf{x}$  sufficiently close to the data manifold and sufficiently small  $t$  the score  $\nabla_{\mathbf{x}} \ln p_t(\mathbf{x})$  points directly at the manifold. We demonstrate this by showing that projection of the score in any direction  $\boldsymbol{\nu} \perp \mathbf{n}$  vanishes in proportion to the projection on  $\mathbf{n} = \frac{(\pi(\mathbf{x})-\mathbf{x})}{\|\pi(\mathbf{x})-\mathbf{x}\|}$  as  $t \rightarrow 0$ . Then Theorem 5.1 and Corollary 5.2 will follow easily from this result.

**Theorem D.1.** *Suppose that the support of the data distribution  $P_0$  is contained in a compact embedded sub-manifold  $\mathcal{M} \subseteq \mathbb{R}^d$  and let  $P_t$  be the distribution of samples from  $P_0$  diffused for time  $t$ . Then, under mild assumptions, for any point  $\mathbf{x} \in \mathbb{R}^d$  sufficiently close to  $\mathcal{M}$ , with orthogonal projection on  $\mathcal{M}$ , given by  $\pi(\mathbf{x})$ . Let  $\mathbf{n}$  be a unit vector pointing from  $\mathbf{x}$  to  $\pi(\mathbf{x})$ , then we have that for any unit vector  $\boldsymbol{\nu}$  orthogonal to  $\mathbf{n}$ :*

$$\frac{\boldsymbol{\nu}^T \nabla_{\mathbf{x}} \ln p_t(\mathbf{x})}{\mathbf{n}^T \nabla_{\mathbf{x}} \ln p_t(\mathbf{x})} \rightarrow 0, \text{ as } t \rightarrow 0.$$

### Assumptions

1. The distribution  $P_0$  has a smooth density  $p_0$  wrt the volume measure on the manifold.
2. The density  $p_0$  is bounded away from zero on the manifold.

### Illustrative simple case

We first present an illustrative proof of a simple case of  $\mathcal{M}$  being a linear subspace with  $k = 1$  and  $d = 2$ . This case gives all of the essential ideas behind the general proof without much of the technicality. For the more interested reader, we then provide a proof of the result for a general manifold, using tools such as the notion of tubular neighbourhoods and some results from Morse theory.

Without the loss of generality assume that  $\mathcal{M} = \{(x_1, x_2) \in \mathbb{R}^2 : x_2 = 0\}$  the line given by the  $x_1$ -axis. Pick a point  $\mathbf{x} \in \mathbb{R}^2$ . The score at point  $\mathbf{x}$  is given by

$$\nabla_{\mathbf{x}} \ln p_t(\mathbf{x}) = \frac{1}{\sigma_t^2 p_t(\mathbf{x})} \int_{\mathcal{M}} (\mathbf{y} - \mathbf{x}) \mathcal{N}(\mathbf{y}|\mathbf{x}, \sigma_t^2 \mathbf{I}) p_0(\mathbf{y}) d\mathbf{y}.$$

Notice that  $\mathcal{N}((y_1, y_2)|(x_1, x_2), \sigma_t^2 \mathbf{I})$ <sup>6</sup> is a bivariate normal distribution and its restriction to  $\mathcal{M}$  is equal to  $\mathcal{N}((y_1, 0)|(x_1, x_2), \sigma_t^2 \mathbf{I}) = \mathcal{N}(0|x_2, \sigma_t^2) \mathcal{N}(y_1|x_1, \sigma_t^2)$ . Therefore

$$\nabla_{\mathbf{x}} \ln p_t(\mathbf{x}) = \frac{\mathcal{N}(0|x_2, \sigma_t^2)}{\sigma_t^2 p_t(\mathbf{x})} \int_{\mathcal{M}} (\mathbf{y} - \mathbf{x}) \mathcal{N}(y_1|x_1, \sigma_t^2) p_0(\mathbf{y}) d\mathbf{y}.$$

This means that the score is the weighted average of vectors pointing from  $\mathbf{x}$  to  $\mathbf{y}$  over all choices of points  $\mathbf{y}$  on the manifold, with weights given by  $w(\mathbf{y}; \sigma_t) := \mathcal{N}(y_1|x_1, \sigma_t^2) p_0(\mathbf{y})$  (see Figure 6 for visual explanation). For small  $\sigma_t$  these weights concentrate around  $\pi(\mathbf{x}) = (x_1, 0)$  the projection of  $\mathbf{x}$

<sup>6</sup>In component-wise notation  $\mathbf{y} = (y_1, y_2)$  and  $\mathbf{x} = (x_1, x_2)$ .

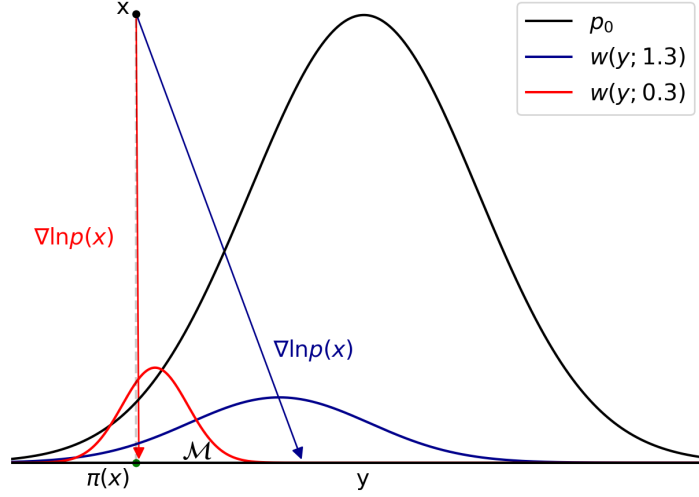


Figure 6: The score is the weighted average of vectors pointing from  $\mathbf{x}$  to  $\mathbf{y}$  with weights given by  $w(\mathbf{y}; \sigma_t)$ . As  $\sigma_t$  decreases weights  $w(\mathbf{y}; \sigma_t)$  concentrate around  $\pi(\mathbf{x})$  and the influence of points  $\mathbf{y}$  away from projection  $\pi(\mathbf{x})$  becomes insignificant. Therefore, the direction of the score tends to align with  $\pi(\mathbf{x}) - \mathbf{x}$ . (Norm of the score vectors on the figure was scaled for better visibility. The direction is preserved.)

on  $\mathcal{M}$ , and vanishing far away from it. Consider a ratio of the tangential part to the normal part of the score:

$$\begin{aligned} \frac{\boldsymbol{\nu}^T \nabla_{\mathbf{x}} \ln p_t(\mathbf{x})}{\mathbf{n}^T \nabla_{\mathbf{x}} \ln p_t(\mathbf{x})} &= \frac{\int_{\mathcal{M}} \boldsymbol{\nu}^T(\mathbf{y} - \mathbf{x}) \mathcal{N}(y_1 | x_1, \sigma_t^2) p_0(\mathbf{y}) d\mathbf{y}}{\int_{\mathcal{M}} \mathbf{n}^T(\mathbf{y} - \mathbf{x}) \mathcal{N}(y_1 | x_1, \sigma_t^2) p_0(\mathbf{y}) d\mathbf{y}} \xrightarrow{\sigma_t \rightarrow 0} \frac{\int_{\mathcal{M}} \boldsymbol{\nu}^T(\mathbf{y} - \mathbf{x}) \delta_{x_1}(y_1) p_0(\mathbf{y}) d\mathbf{y}}{\int_{\mathcal{M}} \mathbf{n}^T(\mathbf{y} - \mathbf{x}) \delta_{x_1}(y_1) p_0(\mathbf{y}) d\mathbf{y}} \\ &= \frac{\boldsymbol{\nu}^T((x_1, 0) - \mathbf{x})}{\mathbf{n}^T((x_1, 0) - \mathbf{x})} = \frac{(1, 0)^T(0, -x_2)}{(0, 1)^T(0, -x_2)} = 0 \end{aligned}$$

where  $\boldsymbol{\nu}$  and  $\mathbf{n}$  are unit vectors in tangential and normal directions respectively. This implies,

$$\begin{aligned} S_{\cos}(\mathbf{n}, \nabla_{\mathbf{x}} \ln p_t(\mathbf{x})) &= \frac{\mathbf{n}^T \nabla_{\mathbf{x}} \ln p_t(\mathbf{x})}{\|\nabla_{\mathbf{x}} \ln p_t(\mathbf{x})\|} = \frac{\mathbf{n}^T \nabla_{\mathbf{x}} \ln p_t(\mathbf{x})}{\sqrt{(\mathbf{n}^T \nabla_{\mathbf{x}} \ln p_t(\mathbf{x}))^2 + (\boldsymbol{\nu}^T \nabla_{\mathbf{x}} \ln p_t(\mathbf{x}))^2}} \\ &= \frac{1}{\sqrt{1 + \left(\frac{\boldsymbol{\nu}^T \nabla_{\mathbf{x}} \ln p_t(\mathbf{x})}{\mathbf{n}^T \nabla_{\mathbf{x}} \ln p_t(\mathbf{x})}\right)^2}} \xrightarrow{t \rightarrow 0} 1. \end{aligned}$$

This establishes the theorem for the simple case. The corollary follows immediately since in the simple case we have  $\mathbf{T} = \boldsymbol{\nu}^T$  and  $\mathbf{N} = \mathbf{n}^T$ .  $\square$

### Deriving the formula for the density of $P_t$

Let  $\mathcal{M}$  be a compact  $k$ -dimensional manifold embedded in  $\mathbb{R}^d$ . Let  $A \subseteq \mathbb{R}^d$ . We define the measure  $P_0$  on  $\mathbb{R}^d$  as

$$P_0(A) := \int_{A \cap \mathcal{M}} p_0(\mathbf{y}) d\mathbf{y} \quad (7)$$

where  $d\mathbf{y}$  is the volume form<sup>7</sup> on  $\mathcal{M}$  and  $p_0$  is a smooth function on  $\mathcal{M}$ <sup>8</sup> such that  $\int_{\mathcal{M}} p_0(\mathbf{y}) d\mathbf{y} = 1$ . Let  $f : \mathbb{R}^d \rightarrow \mathbb{R}$  be a  $P_0$ -measurable function. By approximating  $f$  with simple functions (linear

<sup>7</sup>Integrating over  $A$  using the volume form of  $\mathcal{M}$  can be thought of as taking an appropriately re-scaled Lebesgue integral over  $A$ . That is  $P_0(A) = \int_{A \cap \mathcal{M}} p_0(\mathbf{y}) d\mathbf{y} = \int_A \int_{\mathbb{R}^d} \delta(\mathbf{s} - \mathbf{y}) \hat{p}_0(\mathbf{s}) d\mathbf{s} d\mathbf{y}$ . Where the latter are real Lebesgue integrals and  $\hat{p}_0(\mathbf{s}) = p_0(\mathbf{s})$  for  $\mathbf{s} \in \mathcal{M}$  and zero otherwise.

<sup>8</sup>i.e. for any chart  $\phi : \mathbb{R}^k \supseteq U \rightarrow \mathcal{M}$  the composition  $p_0 \circ \phi : \mathbb{R}^k \supseteq U \rightarrow \mathbb{R}$  is smooth.

combination of indicator functions) we conclude that:

$$\int_A f dP_0 = \int_{A \cap M} f(\mathbf{y}) p_0(\mathbf{y}) d\mathbf{y} \quad (8)$$

Consider a measure  $P_t$  as a convolution of  $P_0$  with a normal distribution on  $\mathbb{R}^d$ . For any measurable  $A \subseteq \mathbb{R}^d$  we have

$$\begin{aligned} (P_0 * \mathcal{N}_{0,t})(A) &:= \int_{\mathbb{R}^d} \int_{A-\mathbf{y}} d\mathcal{N}_{0,t}(\mathbf{x}) dP_0(\mathbf{y}) = \int_{\mathbb{R}^d} \int_{A-\mathbf{y}} \mathcal{N}(\mathbf{x}|0, \sigma_t^2 \mathbf{I}) d\mathbf{x} dP_0(\mathbf{y}) \\ &= \int_{\mathbb{R}^d} \int_A \mathcal{N}(\mathbf{x} - \mathbf{y}|0, \sigma_t^2 \mathbf{I}) d\mathbf{x} dP_0(\mathbf{y}) = \int_{\mathbb{R}^d} \int_A \mathcal{N}(\mathbf{y}|\mathbf{x}, \sigma_t^2 \mathbf{I}) d\mathbf{x} dP_0(\mathbf{y}) \\ &= \int_A \int_{\mathbb{R}^d} \mathcal{N}(\mathbf{y}|\mathbf{x}, \sigma_t^2 \mathbf{I}) dP_0(\mathbf{y}) d\mathbf{x} \stackrel{(8)}{=} \int_A \int_{\mathcal{M}} \mathcal{N}(\mathbf{y}|\mathbf{x}, \sigma_t^2 \mathbf{I}) p_0(\mathbf{y}) d\mathbf{y} d\mathbf{x} \end{aligned}$$

where  $d\mathbf{y}$  is a volume form on  $M$  and  $d\mathbf{x}$  is a volume form on  $\mathbb{R}^d$ . Therefore the measure  $P_t$  has a density on  $\mathbb{R}^d$  given by:

$$p_t(\mathbf{x}) = \int_{\mathcal{M}} \mathcal{N}(\mathbf{y}|\mathbf{x}, \sigma_t^2 \mathbf{I}) p_0(\mathbf{y}) d\mathbf{y}. \quad (9)$$

Note the  $\mathcal{N}(\mathbf{y}|\mathbf{x}, \sigma_t^2 \mathbf{I})$  here. Typically one would write this as  $\mathcal{N}(\mathbf{x}|\mathbf{y}, \sigma_t^2 \mathbf{I})$  and think of (9) as the quantity of probability mass at point  $\mathbf{x}$  after diffusing for time  $t$  with initial distribution  $p_0(\mathbf{y})$ . We instead write it this way as it will be more intuitive to think of (9) as the average probability mass that intersects the manifold after diffusing from a delta distribution at  $\mathbf{x}$  (where the average is taken over  $p_0(\mathbf{y})$ ). These are of course equivalent as  $\mathcal{N}(\mathbf{x}|\mathbf{y}, \sigma_t^2 \mathbf{I})$  is symmetric in  $\mathbf{x}$  and  $\mathbf{y}$ .

### Tubular Neighbourhoods

First we need to ensure that the point  $\mathbf{x}$  has a unique projection on  $\mathcal{M}$ . This is always true for an  $\mathbf{x}$  sufficiently close to  $\mathcal{M}$ . We can formalize this with the notion of *tubular neighbourhood* - a tube around  $\mathcal{M}$  such that every point  $\mathbf{x}$  inside can be uniquely represented as a sum of the point on the manifold and a vector from the normal bundle i.e.  $\mathbf{x} = \mathbf{y} + \mathbf{v}$  where  $\mathbf{y} \in \mathcal{M}$  and  $\mathbf{v} \in \mathcal{N}_{\mathbf{y}}\mathcal{M}$ . Formally:

**Definition D.2.** Endpoint Map

The endpoint map  $Y : \mathcal{N}\mathcal{M} \rightarrow \mathbb{R}^d$  is defined by  $Y(\mathbf{y}, \mathbf{v}) = \mathbf{y} + \mathbf{v}$  for  $\mathbf{y} \in \mathcal{M}$  and  $\mathbf{v} \in \mathcal{N}_{\mathbf{y}}\mathcal{M}$ .

**Definition D.3.** Tubular Neighbourhood

A (uniform) tubular neighbourhood of  $\mathcal{M}$  is a neighbourhood  $U_R$  of  $\mathcal{M}$  in  $\mathbb{R}^d$  that is a diffeomorphic image under the endpoint map of an open subset  $V_R \subseteq \mathcal{N}\mathcal{M}$  of the form:

$$V_R = \{(\mathbf{y}, \mathbf{v}) \in \mathcal{N}\mathcal{M} : \|\mathbf{v}\|_2 < R\}$$

Since  $Y$  restricted to  $V_R$  is a diffeomorphism<sup>9</sup>, it follows that every point  $\mathbf{x} = (\mathbf{y}, \mathbf{v})$  in the tubular neighbourhood has a unique orthogonal projection on  $\mathcal{M}$  given by  $\mathbf{y}$ . We will denote this projection as  $\pi(\mathbf{x})$ .

Conveniently, it turns out that every compact embedded submanifold of  $\mathbb{R}^d$  has a tubular neighbourhood.

**Theorem D.4.** *Tubular Neighborhood Theorem [Lee, 2019, Theorem 5.25]*

*Every compact embedded submanifold of  $\mathbb{R}^d$  has a uniform tubular neighborhood.*

### Preliminary lemmas and Morse theory

In this section we will establish that for every  $\mathbf{x}$  in the tubular neighbourhood of  $\mathcal{M}$  there exists an open neighbourhood  $E$  of  $\pi(\mathbf{x})$  such that:

1.  $\mathbf{n}^T(\mathbf{y} - \mathbf{x}) > \|\pi(\mathbf{x}) - \mathbf{x}\|_2 - \varepsilon$  on  $E$ .
2.  $|\boldsymbol{\nu}^T(\mathbf{y} - \mathbf{x})| < \varepsilon$  on  $E$ .

---

<sup>9</sup>so in particular it is a bijection

3. The mass of a Gaussian centred at  $\mathbf{x}$  is concentrated in  $E$ ,

$$\frac{\int_{\mathcal{M} \setminus E} \mathcal{N}(\mathbf{y}|\mathbf{x}, \sigma_t^2 \mathbf{I}) d\mathbf{y}}{\int_E \mathcal{N}(\mathbf{y}|\mathbf{x}, \sigma_t^2 \mathbf{I}) d\mathbf{y}} \rightarrow 0 \text{ as } t \rightarrow 0.$$

We begin by defining an  $E$  which satisfies the first two conditions.

**Lemma D.5.** *Choose  $E$  contained in a ball of radius  $0 < \varepsilon < \|\mathbf{x} - \pi(\mathbf{x})\|$  around  $\pi(\mathbf{x})$ . Let  $\mathbf{y} \in E$ , and let  $\mathbf{v}_\varepsilon := \mathbf{y} - \pi(\mathbf{x})$ . Then*

1.  $\mathbf{n}^T(\mathbf{y} - \mathbf{x}) > \|\pi(\mathbf{x}) - \mathbf{x}\|_2 - \varepsilon$  on  $E$ .
2.  $|\boldsymbol{\nu}^T(\mathbf{y} - \mathbf{x})| < \varepsilon$  on  $E$ .

*Proof.* By direct computation

$$\begin{aligned} \mathbf{n}^T(\mathbf{y} - \mathbf{x}) &= \mathbf{n}^T((\mathbf{x} - \pi(\mathbf{x})) + \mathbf{v}_\varepsilon) \\ &= \mathbf{n}^T(\mathbf{x} - \pi(\mathbf{x})) + \mathbf{n}^T \mathbf{v}_\varepsilon \\ &= \|\mathbf{x} - \pi(\mathbf{x})\|_2 + \mathbf{n}^T \mathbf{v}_\varepsilon \\ &\geq \|\mathbf{x} - \pi(\mathbf{x})\| - \|\mathbf{v}_\varepsilon\|_2. \end{aligned}$$

We have that  $\|\mathbf{v}_\varepsilon\| < \varepsilon$ , hence for all  $\mathbf{y}$  in  $E$  we have that  $\mathbf{n}^T(\mathbf{y} - \mathbf{x}) \geq \|\mathbf{x} - \pi(\mathbf{x})\| - \varepsilon > 0$ . For the second inequality

$$\begin{aligned} |\boldsymbol{\nu}^T(\mathbf{y} - \mathbf{x})| &\leq |\boldsymbol{\nu}^T((\mathbf{x} - \pi(\mathbf{x})))| + |\boldsymbol{\nu}^T \mathbf{v}_\varepsilon| \\ &\leq \|\mathbf{v}_\varepsilon\|_2 \\ &\leq \varepsilon. \end{aligned}$$

□

Now to find  $E$  which also satisfies the last condition we proceed by recalling some elementary definitions and results of Morse theory.

**Theorem D.6.** *Morse lemma [Nicolaescu, 2011, Corollary 1.17]*

*If  $\mathbf{y}_0$  is a non-degenerate critical point of index  $\gamma$  of a smooth function  $f : \mathcal{M} \rightarrow \mathbb{R}$ , then there exist a chart  $\phi = (\phi_i)_{i=1}^k$  in a neighbourhood  $U$  of  $\mathbf{y}_0$  such that  $\phi(\mathbf{y}_0) = 0$ , and in this chart we have the equality:*

$$f(\mathbf{y}) = f(\mathbf{y}_0) - \sum_{i=1}^{\gamma} \phi_i(\mathbf{y})^2 + \sum_{i=\gamma+1}^k \phi_i(\mathbf{y})^2$$

Let  $f_{\mathbf{x}}(\mathbf{y}) : \mathcal{M} \rightarrow \mathbb{R}$  denote the squared distance function from  $\mathbf{x}$  given by  $f_{\mathbf{x}}(\mathbf{y}) = \|\mathbf{x} - \mathbf{y}\|_2^2$ . We will establish that if  $\mathbf{x}$  is in a tubular neighbourhood, then its projection  $\pi(\mathbf{x})$  is a non-degenerate critical point of  $f_{\mathbf{x}}$  of index zero.

**Definition D.7.** Focal point

A point  $\mathbf{x} = Y(\mathbf{y}, \mathbf{v})$  in the image of the endpoint map  $Y$ , is called a non-focal point of  $\mathcal{M}$  with respect to  $\mathbf{y}$  if  $dY(\mathbf{y}, \mathbf{v})$  is an isomorphism. Otherwise it is called a focal point.

**Theorem D.8.** *Critical points and focal points [Palais and Terng, 1988, Theorem 4.2.6]*

*Let  $\mathcal{M}$  be an embedded submanifold of  $\mathbb{R}^d$ ,  $\mathbf{y} \in M$ ,  $\mathbf{v} \in \mathcal{N}_{\mathbf{y}}\mathcal{M}$ , and  $\mathbf{x} = Y(\mathbf{y}, \mathbf{v}) = \mathbf{y} + \mathbf{v}$ . Then*

1.  $\mathbf{y}$  is a critical point of  $f_{\mathbf{x}}$ .
2.  $\mathbf{y}$  is a non-degenerate critical point of  $f_{\mathbf{x}}$  if and only if  $\mathbf{x}$  is a non-focal point.
3. Index of  $f_{\mathbf{x}}$  at  $\mathbf{y}$  is equal to the number of focal points of  $\mathcal{M}$  with respect to  $\mathbf{y}$  on the line segment joining  $\mathbf{y}$  to  $\mathbf{x}$ .

Because the restriction of the endpoint map  $Y$  to the tubular neighbourhood is a diffeomorphism, the differential  $dY$  is an isomorphism for every point in the tubular neighbourhood. Therefore there are no focal points of  $\mathcal{M}$  in the tubular neighbourhood. Hence, it follows directly from the above theorem, that if  $\mathbf{x}$  is in the tubular neighbourhood, then the projection  $\pi(\mathbf{x})$  is a non-degenerate critical point of  $f_{\mathbf{x}}$  of index zero. Now we are ready to prove the following lemma.

**Lemma D.9.** *There exists a connected open neighbourhood  $E$  of  $\pi(\mathbf{x})$  satisfying conditions of lemma D.5 and such that,*

$$\frac{\int_{\mathcal{M} \setminus E} \mathcal{N}(\mathbf{y}|\mathbf{x}, \sigma_t^2 \mathbf{I}) d\mathbf{y}}{\int_E \mathcal{N}(\mathbf{y}|\mathbf{x}, \sigma_t^2 \mathbf{I}) d\mathbf{y}} \rightarrow 0 \text{ as } t \rightarrow 0. \quad (10)$$

*Proof.* Fix  $\varepsilon > 0$ . Then conditions of lemma D.5 are satisfied inside  $B(\pi(\mathbf{x}), \varepsilon)$ . We have demonstrated that  $\pi(\mathbf{x})$  fulfills the criteria stipulated by the Morse lemma. Consequently, we can pick  $\tilde{U}$  as the neighborhood and  $\phi$  as the coordinate system that the Morse lemma provides. Now let  $U = \tilde{U} \cap B(\pi(\mathbf{x}), \varepsilon)$ . Since  $\mathcal{M}$  is compact and  $U$  is open, there exists  $m = \min_{\mathcal{M} \setminus U} f_{\mathbf{x}}(\mathbf{y})$  and by uniqueness of projection  $f_{\mathbf{x}}(\pi(\mathbf{x})) < m$ . Let  $r = \sqrt{m - (f_{\mathbf{x}}(\pi(\mathbf{x})))}/2$  and let  $E = \phi^{-1}(B(0, r))$ . For all  $\mathbf{y} \in E$  we have:

$$f_{\mathbf{x}}(\mathbf{y}) = f_{\mathbf{x}}(\pi(\mathbf{x})) + \|\phi(\mathbf{y})\|^2 < f_{\mathbf{x}}(\pi(\mathbf{x})) + r^2 < m.$$

Notice that for every  $\mathbf{y} \in U \setminus E$  we have  $f_{\mathbf{x}}(\mathbf{y}) \geq f_{\mathbf{x}}(\pi(\mathbf{x})) + r^2$ . Therefore we have established that

$$\forall \mathbf{y} \in E \forall \tilde{\mathbf{y}} \in \mathcal{M} \setminus E f_{\mathbf{x}}(\mathbf{y}) < f_{\mathbf{x}}(\tilde{\mathbf{y}}). \quad (11)$$

Computing directly, we have

$$\frac{\int_{\mathcal{M} \setminus E} \mathcal{N}(\mathbf{y}|\mathbf{x}, \sigma_t^2 \mathbf{I}) d\mathbf{y}}{\int_E \mathcal{N}(\mathbf{y}|\mathbf{x}, \sigma_t^2 \mathbf{I}) d\mathbf{y}} = \frac{\int_{\mathcal{M} \setminus E} \exp\{-f_{\mathbf{x}}(\mathbf{y})/2\sigma_t^2\} d\mathbf{y}}{\int_E \exp\{-f_{\mathbf{x}}(\mathbf{y})/2\sigma_t^2\} d\mathbf{y}} \quad (12)$$

By the mean value theorem there exists  $\mathbf{y}^* \in E$  and  $\tilde{\mathbf{y}}^* \in \mathcal{M} \setminus E$  such that

$$\begin{aligned} \int_E \exp\{-f_{\mathbf{x}}(\mathbf{y})/2\sigma_t^2\} d\mathbf{y} &= \text{Vol}(E) \exp\{-f_{\mathbf{x}}(\mathbf{y}^*)/2\sigma_t^2\} \\ \int_{\mathcal{M} \setminus E} \exp\{-f_{\mathbf{x}}(\mathbf{y})/2\sigma_t^2\} d\mathbf{y} &= \text{Vol}(\mathcal{M} \setminus E) \exp\{-f_{\mathbf{x}}(\tilde{\mathbf{y}}^*)/2\sigma_t^2\} \end{aligned}$$

We can use this to evaluate (12) to give,

$$\frac{\int_{\mathcal{M} \setminus E} \mathcal{N}(\mathbf{y}|\mathbf{x}, \sigma_t^2 \mathbf{I}) d\mathbf{y}}{\int_E \mathcal{N}(\mathbf{y}|\mathbf{x}, \sigma_t^2 \mathbf{I}) d\mathbf{y}} = \frac{\text{Vol}(\mathcal{M} \setminus E) \exp\{-f_{\mathbf{x}}(\tilde{\mathbf{y}}^*)/2\sigma_t^2\}}{\text{Vol}(E) \exp\{-f_{\mathbf{x}}(\mathbf{y}^*)/2\sigma_t^2\}} = \frac{\text{Vol}(\mathcal{M} \setminus E)}{\text{Vol}(E)} \exp\left\{-\frac{f_{\mathbf{x}}(\tilde{\mathbf{y}}^*) - f_{\mathbf{x}}(\mathbf{y}^*)}{2\sigma_t^2}\right\}$$

Since by (11)  $f_{\mathbf{x}}(\tilde{\mathbf{y}}^*) - f_{\mathbf{x}}(\mathbf{y}^*) > 0$  the above goes to zero as  $\sigma_t$  goes to zero. Moreover, since  $E \subseteq U \subseteq B(\pi(\mathbf{x}), \varepsilon)$ , the conditions of lemma D.5 are also satisfied.  $\square$

### Proof of Theorem D.1

Fix  $\varepsilon > 0$ . Assume that  $\mathbf{x}$  is in a tubular neighbourhood of  $\mathcal{M}$ , so that the projection  $\pi(\mathbf{x})$  exists.

$$\frac{\boldsymbol{\nu}^T \nabla_{\mathbf{x}} \ln p_t(\mathbf{x})}{\mathbf{n}^T \nabla_{\mathbf{x}} \ln p_t(\mathbf{x})} = \frac{\boldsymbol{\nu}^T \nabla_{\mathbf{x}} p_t(\mathbf{x})}{\mathbf{n}^T \nabla_{\mathbf{x}} p_t(\mathbf{x})} = \frac{\int_{\mathcal{M}} \boldsymbol{\nu}^T(\mathbf{y} - \mathbf{x}) \mathcal{N}(\mathbf{y}|\mathbf{x}, \sigma_t^2 \mathbf{I}) p_0(\mathbf{y}) d\mathbf{y}}{\int_{\mathcal{M}} \mathbf{n}^T(\mathbf{y} - \mathbf{x}) \mathcal{N}(\mathbf{y}|\mathbf{x}, \sigma_t^2 \mathbf{I}) p_0(\mathbf{y}) d\mathbf{y}} \quad (13)$$

Split  $\mathcal{M}$  into two parts:  $E$  and  $\mathcal{M} \setminus E$ , where  $E = B(\mathbf{x}, r) \cap \mathcal{M}$  is an open neighbourhood of  $\pi(\mathbf{x})$  in  $\mathcal{M}$  satisfying the conditions of Lemma D.9 and Lemma D.5 for a chosen  $\varepsilon > 0$ , then we have that (13) is equal to

$$\frac{\int_E \boldsymbol{\nu}^T(\mathbf{y} - \mathbf{x}) \mathcal{N}(\mathbf{y}|\mathbf{x}, \sigma_t^2 \mathbf{I}) p_0(\mathbf{y}) d\mathbf{y}}{\int_{\mathcal{M}} \mathbf{n}^T(\mathbf{y} - \mathbf{x}) \mathcal{N}(\mathbf{y}|\mathbf{x}, \sigma_t^2 \mathbf{I}) p_0(\mathbf{y}) d\mathbf{y}} + \frac{\int_{\mathcal{M} \setminus E} \boldsymbol{\nu}^T(\mathbf{y} - \mathbf{x}) \mathcal{N}(\mathbf{y}|\mathbf{x}, \sigma_t^2 \mathbf{I}) p_0(\mathbf{y}) d\mathbf{y}}{\int_{\mathcal{M}} \mathbf{n}^T(\mathbf{y} - \mathbf{x}) \mathcal{N}(\mathbf{y}|\mathbf{x}, \sigma_t^2 \mathbf{I}) p_0(\mathbf{y}) d\mathbf{y}}. \quad (14)$$

We begin by bounding the first term:

$$\begin{aligned} \frac{\int_E \boldsymbol{\nu}^T(\mathbf{y} - \mathbf{x}) \mathcal{N}(\mathbf{y}|\mathbf{x}, \sigma_t^2 \mathbf{I}) p_0(\mathbf{y}) d\mathbf{y}}{\int_{\mathcal{M}} \mathbf{n}^T(\mathbf{y} - \mathbf{x}) \mathcal{N}(\mathbf{y}|\mathbf{x}, \sigma_t^2 \mathbf{I}) p_0(\mathbf{y}) d\mathbf{y}} &= \frac{\int_E \boldsymbol{\nu}^T(\mathbf{y} - \mathbf{x}) \mathcal{N}(\mathbf{y}|\mathbf{x}, \sigma_t^2 \mathbf{I}) p_0(\mathbf{y}) d\mathbf{y}}{\int_E \mathbf{n}^T(\mathbf{y} - \mathbf{x}) \mathcal{N}(\mathbf{y}|\mathbf{x}, \sigma_t^2 \mathbf{I}) p_0(\mathbf{y}) d\mathbf{y} + \int_{\mathcal{M} \setminus E} \mathbf{n}^T(\mathbf{y} - \mathbf{x}) \mathcal{N}(\mathbf{y}|\mathbf{x}, \sigma_t^2 \mathbf{I}) p_0(\mathbf{y}) d\mathbf{y}} \\ &= \frac{\frac{\int_E \boldsymbol{\nu}^T(\mathbf{y} - \mathbf{x}) \mathcal{N}(\mathbf{y}|\mathbf{x}, \sigma_t^2 \mathbf{I}) p_0(\mathbf{y}) d\mathbf{y}}{\int_E \mathbf{n}^T(\mathbf{y} - \mathbf{x}) \mathcal{N}(\mathbf{y}|\mathbf{x}, \sigma_t^2 \mathbf{I}) p_0(\mathbf{y}) d\mathbf{y}}}{1 + \frac{\int_{\mathcal{M} \setminus E} \mathbf{n}^T(\mathbf{y} - \mathbf{x}) \mathcal{N}(\mathbf{y}|\mathbf{x}, \sigma_t^2 \mathbf{I}) p_0(\mathbf{y}) d\mathbf{y}}{\int_E \mathbf{n}^T(\mathbf{y} - \mathbf{x}) \mathcal{N}(\mathbf{y}|\mathbf{x}, \sigma_t^2 \mathbf{I}) p_0(\mathbf{y}) d\mathbf{y}}} =: \frac{A_t}{1 + B_t} \end{aligned}$$

For  $A_t$  we have

$$|A_t| = \left| \frac{\int_E \boldsymbol{\nu}^T(\mathbf{y} - \mathbf{x}) \mathcal{N}(\mathbf{y}|\mathbf{x}, \sigma_t^2 \mathbf{I}) p_0(\mathbf{y}) d\mathbf{y}}{\int_E \mathbf{n}^T(\mathbf{y} - \mathbf{x}) \mathcal{N}(\mathbf{y}|\mathbf{x}, \sigma_t^2 \mathbf{I}) p_0(\mathbf{y}) d\mathbf{y}} \right|.$$

Using the fact that  $\mathbf{n}^T(\mathbf{y} - \mathbf{x})$  is positive and bounded away from zero and applying the triangle inequality we obtain

$$\begin{aligned} |A_t| &\leq \frac{\int_E |\boldsymbol{\nu}^T(\mathbf{y} - \mathbf{x})| \mathcal{N}(\mathbf{y}|\mathbf{x}, \sigma_t^2 \mathbf{I}) p_0(\mathbf{y}) d\mathbf{y}}{\int_E \mathbf{n}^T(\mathbf{y} - \mathbf{x}) \mathcal{N}(\mathbf{y}|\mathbf{x}, \sigma_t^2 \mathbf{I}) p_0(\mathbf{y}) d\mathbf{y}} \\ &\leq \frac{\varepsilon p_{\max} \int_E \mathcal{N}(\mathbf{y}|\mathbf{x}, \sigma_t^2 \mathbf{I}) d\mathbf{y}}{(\|\pi(\mathbf{x}) - \mathbf{x}\| - \varepsilon) p_{\min} \int_E \mathcal{N}(\mathbf{y}|\mathbf{x}, \sigma_t^2 \mathbf{I}) d\mathbf{y}} \\ &= \frac{p_{\max}}{p_{\min}} \frac{\varepsilon}{\|\pi(\mathbf{x}) - \mathbf{x}\| - \varepsilon}, \end{aligned}$$

where in the second inequality we used that  $0 < p_{\min} < p_0(\mathbf{y}) < p_{\max}$ ,  $|\boldsymbol{\nu}^T(\mathbf{y} - \mathbf{x})| < \varepsilon$  and  $\mathbf{n}^T(\mathbf{y} - \mathbf{x}) > \|\pi(\mathbf{x}) - \mathbf{x}\| - \varepsilon$  on  $E$ . Since  $\varepsilon$  was arbitrary this term can be made arbitrary small. Now we move to  $B_t$ . Let  $D = \max_{\mathbf{y} \in \mathcal{M}} \|\mathbf{x} - \mathbf{y}\|$ , by the triangle and Cauchy Schwarz inequalities we have

$$\begin{aligned} |B_t| &\leq \frac{\int_{\mathcal{M} \setminus E} |\mathbf{n}^T(\mathbf{y} - \mathbf{x})| \mathcal{N}(\mathbf{y}|\mathbf{x}, \sigma_t^2 \mathbf{I}) p_0(\mathbf{y}) d\mathbf{y}}{\int_E \mathbf{n}^T(\mathbf{y} - \mathbf{x}) \mathcal{N}(\mathbf{y}|\mathbf{x}, \sigma_t^2 \mathbf{I}) p_0(\mathbf{y}) d\mathbf{y}} \\ &\leq \frac{p_{\max} D}{p_{\min} (\|\pi(\mathbf{x}) - \mathbf{x}\| - \varepsilon)} \frac{\int_{\mathcal{M} \setminus E} \mathcal{N}(\mathbf{y}|\mathbf{x}, \sigma_t^2 \mathbf{I}) d\mathbf{y}}{\int_E \mathcal{N}(\mathbf{y}|\mathbf{x}, \sigma_t^2 \mathbf{I}) d\mathbf{y}}. \end{aligned}$$

which goes to zero as  $t$  goes to zero. Finally we move to the second term in (14), we start with the same steps as with the first term

$$\frac{\int_{\mathcal{M} \setminus E} \boldsymbol{\nu}^T(\mathbf{y} - \mathbf{x}) \mathcal{N}(\mathbf{y}|\mathbf{x}, \sigma_t^2 \mathbf{I}) p_0(\mathbf{y}) d\mathbf{y}}{\int_{\mathcal{M}} \mathbf{n}^T(\mathbf{y} - \mathbf{x}) \mathcal{N}(\mathbf{y}|\mathbf{x}, \sigma_t^2 \mathbf{I}) p_0(\mathbf{y}) d\mathbf{y}} = \frac{\frac{\int_{\mathcal{M} \setminus E} \boldsymbol{\nu}^T(\mathbf{y} - \mathbf{x}) \mathcal{N}(\mathbf{y}|\mathbf{x}, \sigma_t^2 \mathbf{I}) p_0(\mathbf{y}) d\mathbf{y}}{\int_E \mathbf{n}^T(\mathbf{y} - \mathbf{x}) \mathcal{N}(\mathbf{y}|\mathbf{x}, \sigma_t^2 \mathbf{I}) p_0(\mathbf{y}) d\mathbf{y}}}{1 + \frac{\int_{\mathcal{M} \setminus E} \mathbf{n}^T(\mathbf{y} - \mathbf{x}) \mathcal{N}(\mathbf{y}|\mathbf{x}, \sigma_t^2 \mathbf{I}) p_0(\mathbf{y}) d\mathbf{y}}{\int_E \mathbf{n}^T(\mathbf{y} - \mathbf{x}) \mathcal{N}(\mathbf{y}|\mathbf{x}, \sigma_t^2 \mathbf{I}) p_0(\mathbf{y}) d\mathbf{y}}} =: \frac{C_t}{1 + B_t}$$

so we only need to examine  $C_t$ . By the triangle and Cauchy Schwarz inequalities again, we have

$$\begin{aligned} |C_t| &\leq \frac{\int_{\mathcal{M} \setminus E} |\boldsymbol{\nu}^T(\mathbf{y} - \mathbf{x})| \mathcal{N}(\mathbf{y}|\mathbf{x}, \sigma_t^2 \mathbf{I}) p_0(\mathbf{y}) d\mathbf{y}}{\int_E \mathbf{n}^T(\mathbf{y} - \mathbf{x}) \mathcal{N}(\mathbf{y}|\mathbf{x}, \sigma_t^2 \mathbf{I}) p_0(\mathbf{y}) d\mathbf{y}} \\ &\leq \frac{p_{\max} D}{p_{\min} (\|\pi(\mathbf{x}) - \mathbf{x}\| - \varepsilon)} \frac{\int_{\mathcal{M} \setminus E} \mathcal{N}(\mathbf{y}|\mathbf{x}, \sigma_t^2 \mathbf{I}) d\mathbf{y}}{\int_E \mathcal{N}(\mathbf{y}|\mathbf{x}, \sigma_t^2 \mathbf{I}) d\mathbf{y}} \end{aligned}$$

which goes to zero as  $t$  goes to zero. Putting all together

$$\begin{aligned} \frac{|\boldsymbol{\nu}^T \nabla_{\mathbf{x}} \ln p_t(\mathbf{x})|}{|\mathbf{n}^T \nabla_{\mathbf{x}} \ln p_t(\mathbf{x})|} &= \frac{|A_t + C_t|}{|1 + B_t|} \\ &\leq \frac{1}{|1 + B_t|} \left( \frac{p_{\max}}{p_{\min}} \frac{\varepsilon}{\|\pi(\mathbf{x}) - \mathbf{x}\| - \varepsilon} + |C_t| \right) \\ &\xrightarrow{t \rightarrow 0} \frac{p_{\max}}{p_{\min}} \frac{\varepsilon}{\|\pi(\mathbf{x}) - \mathbf{x}\| - \varepsilon} \end{aligned}$$

Since  $\varepsilon$  can be chosen arbitrarily small this finishes the proof.  $\square$

### Proof of Theorem 5.1

Beginning with  $\mathbf{n}$  and extending to an orthonormal basis  $(\mathbf{n}, \boldsymbol{\nu}_1, \dots, \boldsymbol{\nu}_{d-1})$  of  $\mathbb{R}^d$ , we have

$$\begin{aligned} S_{\cos}(\mathbf{n}, \nabla_{\mathbf{x}} \ln p_t(\mathbf{x})) &= \frac{\mathbf{n}^T \nabla_{\mathbf{x}} \ln p_t(\mathbf{x})}{\|\nabla_{\mathbf{x}} \ln p_t(\mathbf{x})\|} = \frac{\mathbf{n}^T (\nabla_{\mathbf{x}} \ln p_t(\mathbf{x}))}{\sqrt{(\mathbf{n}^T \nabla_{\mathbf{x}} \ln p_t(\mathbf{x}))^2 + \sum_{i=1}^{d-1} (\boldsymbol{\nu}_i^T \nabla_{\mathbf{x}} \ln p_t(\mathbf{x}))^2}} \\ &= \frac{1}{\sqrt{1 + \sum_{i=1}^{d-1} \left( \frac{\boldsymbol{\nu}_i^T \nabla_{\mathbf{x}} \ln p_t(\mathbf{x})}{\mathbf{n}^T \nabla_{\mathbf{x}} \ln p_t(\mathbf{x})} \right)^2}} \xrightarrow{t \rightarrow 0} 1, \end{aligned}$$

where in taking the limit we applied the Theorem D.1.  $\square$

**Proof of Corollary 5.2**

Let  $(\boldsymbol{\tau}_1, \dots, \boldsymbol{\tau}_k)$  be an orthonormal basis of the tangent space  $T_{\pi(\mathbf{x})}\mathcal{M}$  and extend  $\mathbf{n}$  to an orthonormal basis  $(\mathbf{n}, \boldsymbol{\eta}_1, \dots, \boldsymbol{\eta}_{d-k-1})$  of the normal space  $\mathcal{N}_{\pi(\mathbf{x})}\mathcal{M}$ . Then the projection of the score on the tangent space is given by  $\mathbf{T}\nabla_{\mathbf{x}} \ln p_t(\mathbf{x}) = \sum_{i=1}^k (\boldsymbol{\tau}_i^T \nabla_{\mathbf{x}} \ln p_t(\mathbf{x})) \boldsymbol{\tau}_i$ , while the projection on the normal space is  $\mathbf{N}\nabla_{\mathbf{x}} \ln p_t(\mathbf{x}) = (\mathbf{n}^T \nabla_{\mathbf{x}} \ln p_t(\mathbf{x})) \mathbf{n} + \sum_{i=1}^{d-k-1} (\boldsymbol{\eta}_i^T \nabla_{\mathbf{x}} \ln p_t(\mathbf{x})) \boldsymbol{\eta}_i$ . Therefore

$$\begin{aligned} \frac{\|\mathbf{T}\nabla_{\mathbf{x}} \ln p_t(\mathbf{x})\|}{\|\mathbf{N}\nabla_{\mathbf{x}} \ln p_t(\mathbf{x})\|} &= \sqrt{\frac{\sum_{i=1}^k (\boldsymbol{\tau}_i^T \nabla_{\mathbf{x}} \ln p_t(\mathbf{x}))^2}{(\mathbf{n}^T \nabla_{\mathbf{x}} \ln p_t(\mathbf{x}))^2 + \sum_{i=1}^{d-k-1} (\boldsymbol{\eta}_i^T \nabla_{\mathbf{x}} \ln p_t(\mathbf{x}))^2}} \\ &= \sqrt{\frac{\sum_{i=1}^k \left( \frac{\boldsymbol{\tau}_i^T \nabla_{\mathbf{x}} \ln p_t(\mathbf{x})}{\mathbf{n}^T \nabla_{\mathbf{x}} \ln p_t(\mathbf{x})} \right)^2}{1 + \sum_{i=1}^{d-k-1} \left( \frac{\boldsymbol{\eta}_i^T \nabla_{\mathbf{x}} \ln p_t(\mathbf{x})}{\mathbf{n}^T \nabla_{\mathbf{x}} \ln p_t(\mathbf{x})} \right)^2}} \xrightarrow{t \rightarrow 0} 0 \end{aligned}$$

where in taking the limit we applied the Theorem D.1. □

## E Details on the design of synthetic image manifolds

**Squares image manifold:** We generated the *k-squares dataset* whose intrinsic dimension is controllable and is set to  $k$ . This dataset comprises  $32 \times 32$  pixel images of squares, generated by first establishing fixed square center locations and side lengths (either 3 or 5 units) across all datapoints. For each square in a given image, we uniformly sampled a brightness value from the unit interval for all pixels within the square’s boundary, summing values at points of intersection. The dimension of this manifold is equal to the number of squares  $k$  and the ambient space dimension is  $32 \times 32 = 1024$ . We provide samples in Figure 7.

**Gaussian blobs image manifold:** The Squares image manifold is contained in a low dimensional linear subspace which allowed PPCA to estimate the dimension very well. For this reason, we constructed a synthetic image manifold of known dimension, which cannot be contained in any low dimensional linear subspace. We replace the squares by Gaussian blobs (i.e. brightness of pixels within each blob is proportional to a Gaussian pdf). We randomly pick the centers of the Gaussian blobs which remain fixed for all datapoints. For each datapoint, we sample the standard deviation of each Gaussian blob uniformly from the interval  $[1, 5]$ . The dimension of this manifold is equal to the number of Gaussian blobs. We provide samples in Figure 8.

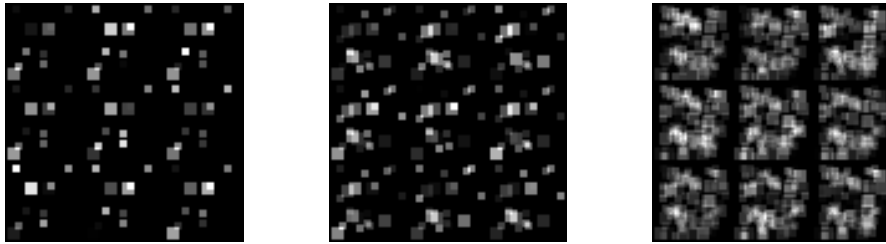


Figure 7: Nine samples from Squares image manifolds of dimensions 10, 20 and 100 (from left to right).

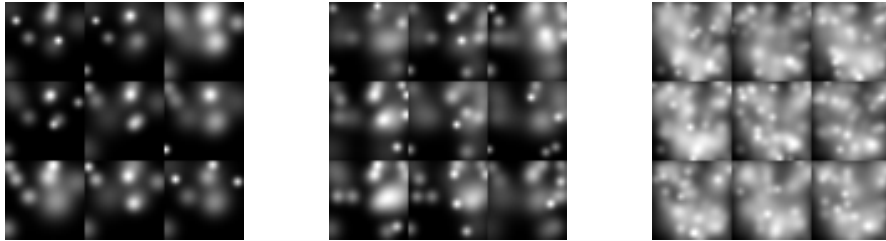


Figure 8: Nine samples from Gaussian blob image manifolds of dimensions 10, 20 and 100 (from left to right).

## F Additional Experimental Results

### F.1 Euclidean Data

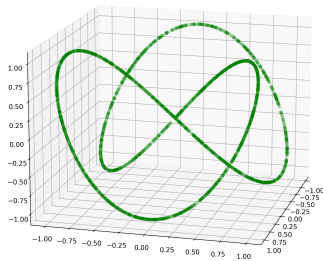


Figure 9: Projection of the spaghetti line on the first three dimensions.

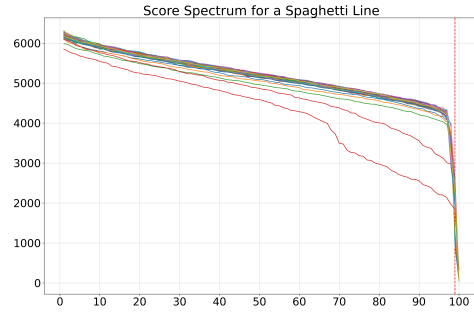


Figure 10: Score spectrum of the spaghetti line. The last singular value clearly vanishes indicating that the intrinsic dimensionality of the manifold is equal to one.

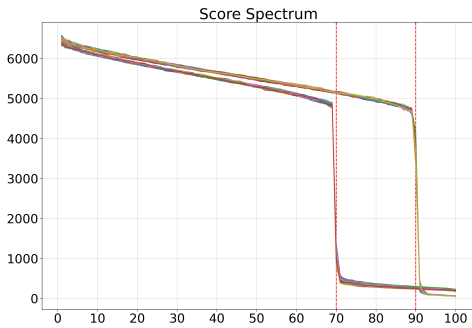


Figure 11: Score spectrum for the union of  $k$ -spheres ( $k_1 = 10, k_2 = 30$ ). The separated drops in the spectra clearly show that the data comes from the union of two manifolds of different dimensions.

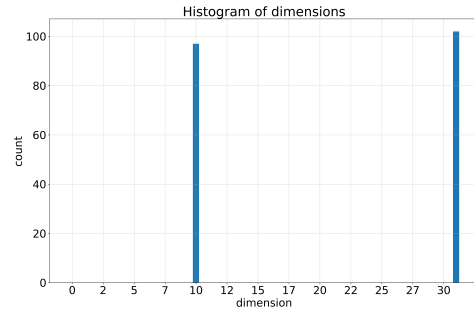


Figure 12: The histogram of estimated dimensions for the union of  $k$ -spheres ( $k_1 = 10, k_2 = 30$ ). The counts are taken over estimates  $\hat{k}(\mathbf{x}_0^{(i)})$  at different points  $\mathbf{x}_0^{(i)}$ .

## E.2 Synthetic Image Data

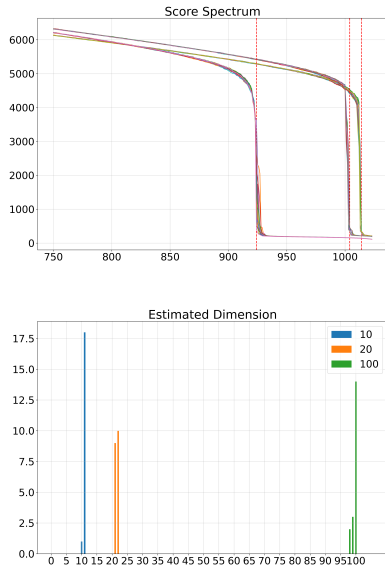


Figure 13: Score spectra and histogram of estimated dimension based on the score spectrum of the Squares image manifold of dimensions 10, 20 and 100.

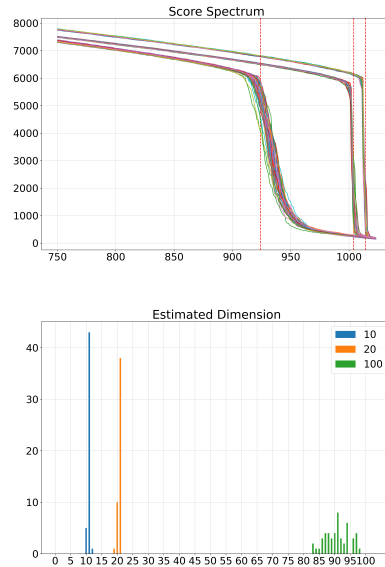


Figure 14: Score spectra and histogram of estimated dimension based on the score spectrum of the Gaussian blobs image manifold of dimensions 10, 20 and 100.

## E.3 MNIST

In Figure 15 we present 500 score spectra evaluated at 500 different instances for each digit. We observe that a considerable number of spectra indicate lower manifold dimension than the dimension documented in Table 1. This deviation can be attributed to amplified geometrical and statistical error at the respective evaluation points.

We choose the maximum estimated dimension as our conjecture of the intrinsic dimension under the premise that a collapse of the spectrum at a smaller dimension than the dimension of the normal space is extremely unlikely from a probabilistic standpoint. However, it is feasible to encounter a spectrum collapse suggesting a higher normal space dimension, hence a lower intrinsic dimension, due to the intensified geometric and approximation error at the point of evaluation. It is noteworthy that our estimation strategy locates the drop at the position of the maximal gradient, a practice that may marginally inflate the intrinsic dimension estimate, as exemplified in the Squares and Gaussian blobs manifolds. Therefore, if our reported dimension for each MNIST digit is not precise, it is either a minor overestimation or a lower limit of the true dimension.

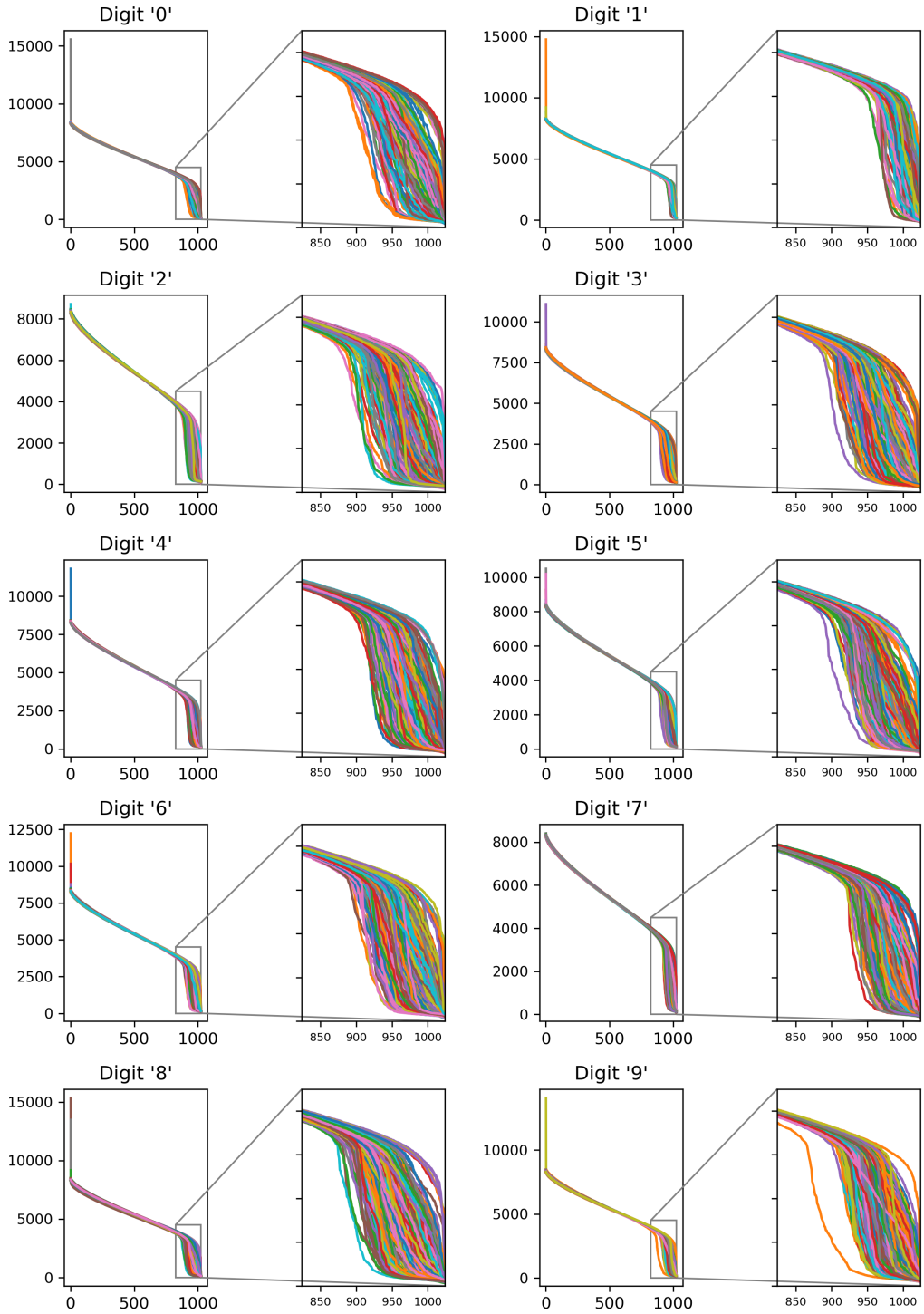


Figure 15: MNIST score spectra for all digits

## G Robustness analysis

### G.1 Robustness to score approximation error

As we discussed in the previous sections, our method is guaranteed to work given a perfect score approximation for sufficiently small  $t$ . However, in practice there will be an approximation error resulting from finite training data, limited model capacity and imperfect optimization. Therefore, we conduct an empirical analysis of the influence of the error in score approximation on the produced estimate of the dimension. We train a model  $s_\theta$  on a uniform distribution on 25-sphere and then we corrupt the output of the model with a Gaussian perturbation  $e \sim \mathcal{N}(0, \sigma_e^2 \mathbf{I})$ . Then, we produce score spectra by applying our method to the resulting corrupted scores. We repeat this experiment for different intensities of noise  $\sigma_e$ . We pick  $\sigma_e$  so that the noise norm to score norm ratio  $r = \mathbb{E}[\|e\|] / \mathbb{E}_{x_{t_0} \sim p_{t_0}(x_{t_0} | x_0)}[\|s(x_{t_0}, t_0)\|]$  has a prescribed value. We find that as we increase the intensity of noise singular values corresponding to the tangential component start to increase causing the gap in the score spectrum to diminish. This is expected since the noise added to the score vectors has a tangential component. However, for values of  $r < 0.5$  our method is still producing a visible drop in the spectrum at the correct point. The results are presented in Figure 16.

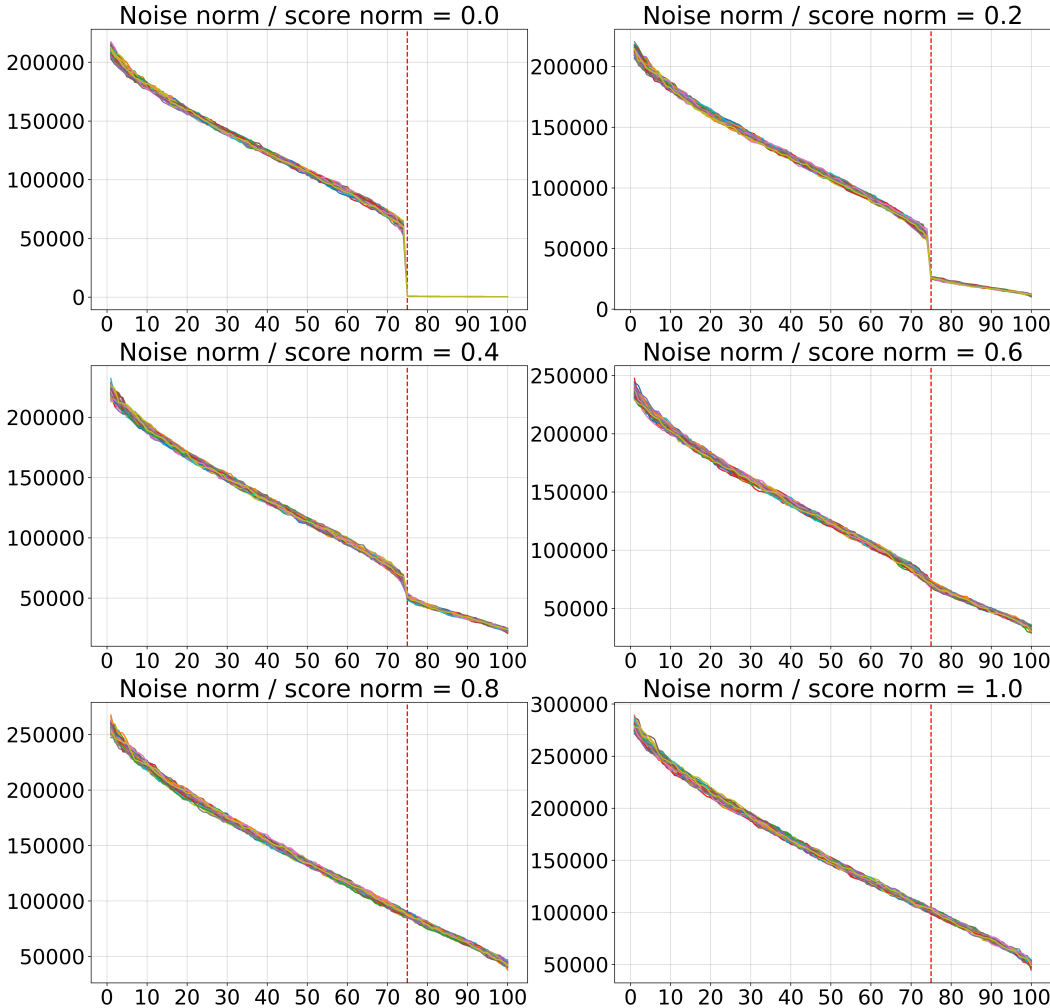


Figure 16: Score spectra for noise corrupted score model on 25-sphere.

## G.2 Robustness to non-uniform distribution on the manifold

	Uniform	$\alpha = 1$	$\alpha = 0.75$	$\alpha = 0.5$
Ground Truth	10	10	10	10
Ours	11	10	10	7
MLE (m=5)	9.61	5.37	4.83	4.12
MLE (m=20)	9.46	4.99	4.49	3.82
Local PCA	11	5	4	3
PPCA	11	11	11	11

Table 4: Dimensionality detection for non-uniform distribution. For our method the maximum over pointwise estimates  $\hat{k}(\mathbf{x}_0)$  is considered.

non-uniformity. Then, we embed the resulting points via a random isometry in a 100 dimensional ambient space. We sample  $n = 1000$  points  $\mathbf{x}_0^{(j)}$  from the manifold and at each point we estimate the dimensionality  $\hat{k}(\mathbf{x}_0^{(j)})$  via the score spectrum. The pointwise estimates are presented in Figure 17 and final estimates are shown in Table 4. For values of  $\alpha \in \{1, 0.75\}$ , we can still obtain an accurate estimate of the dimension if we take  $\hat{k} = \max_{j=1, \dots, 1000} \hat{k}(\mathbf{x}_0^{(j)})$  the maximum over point-wise estimates. For an extremely concentrated distribution with  $\alpha = 0.5$  the method underestimates the dimension, which indicates that the tangential component of the score was not approximately constant in the neighborhoods used to sample the scores. This problem could be further mitigated by approximating the score closer to the manifold and using smaller sampling neighborhoods (i.e. for smaller  $t_0$ ) or sampling more points  $\mathbf{x}_0^{(j)}$ . Notice that taking the maximum over  $\hat{k}(\mathbf{x}_0^{(j)})$  is theoretically justified (as long as we assume we are dealing with a connected manifold) since our method can underestimate due to geometric or approximation error (cf. sections 5 and 6, but it is unlikely to significantly overestimate).

## G.3 Relaxing the strict manifold assumption

The proof of the Theorem 5.1 assumes that  $p_0$  is strictly contained on the data manifold  $\mathcal{M}$ , however in practice it is possible that the data distribution is concentrated around  $\mathcal{M}$  rather than being contained within. Therefore, we conduct an empirical analysis, which examines how our method works in the case of the data contained around the manifold. We start with  $p_0$  a uniform distribution on a unit 25-sphere embedded in a 100 dimensional space and convolve it with a Gaussian distribution  $\mathcal{N}(0, \sigma \mathbf{I})$  to obtain a distribution  $p_0^\sigma$  that concentrates around  $\mathcal{M}$ . As  $\sigma$  increases the distribution is blurred out more and more into the ambient space. We train score model on each of the resulting distributions and use our method to estimate the dimension. We find that our method produces correct estimation for for small values of  $\sigma$  i.e. when  $p_0^\sigma$  is still concentrated tightly around  $\mathcal{M}$ . This is expected since of high values of  $\sigma$  the distribution isn't really concentrated around any manifold and therefore the notion of intrinsic dimension doesn't make any sense. The results are presented in Figure 18.

We examine the robustness to our method to non-uniformity in data distribution on the manifold surface. Under perfect score approximation and sufficiently small  $t_0$  our method is guaranteed to work, but we conduct an empirical study to investigate the behaviour in the presence of score approximation error and  $t_0 > 0$  used in practice in diffusion models. We consider a  $k$ -sphere and sample the surface of the sphere in a non-uniform fashion. We obtain points on the  $k$ -sphere by sampling vectors  $\boldsymbol{\theta}$  of  $k - 1$  angles (in radians) from a Gaussian distribution  $\mathcal{N}(0, \alpha \mathbf{I})$ , where  $\alpha \in \mathbb{R}$  is a constant that determines the degree of

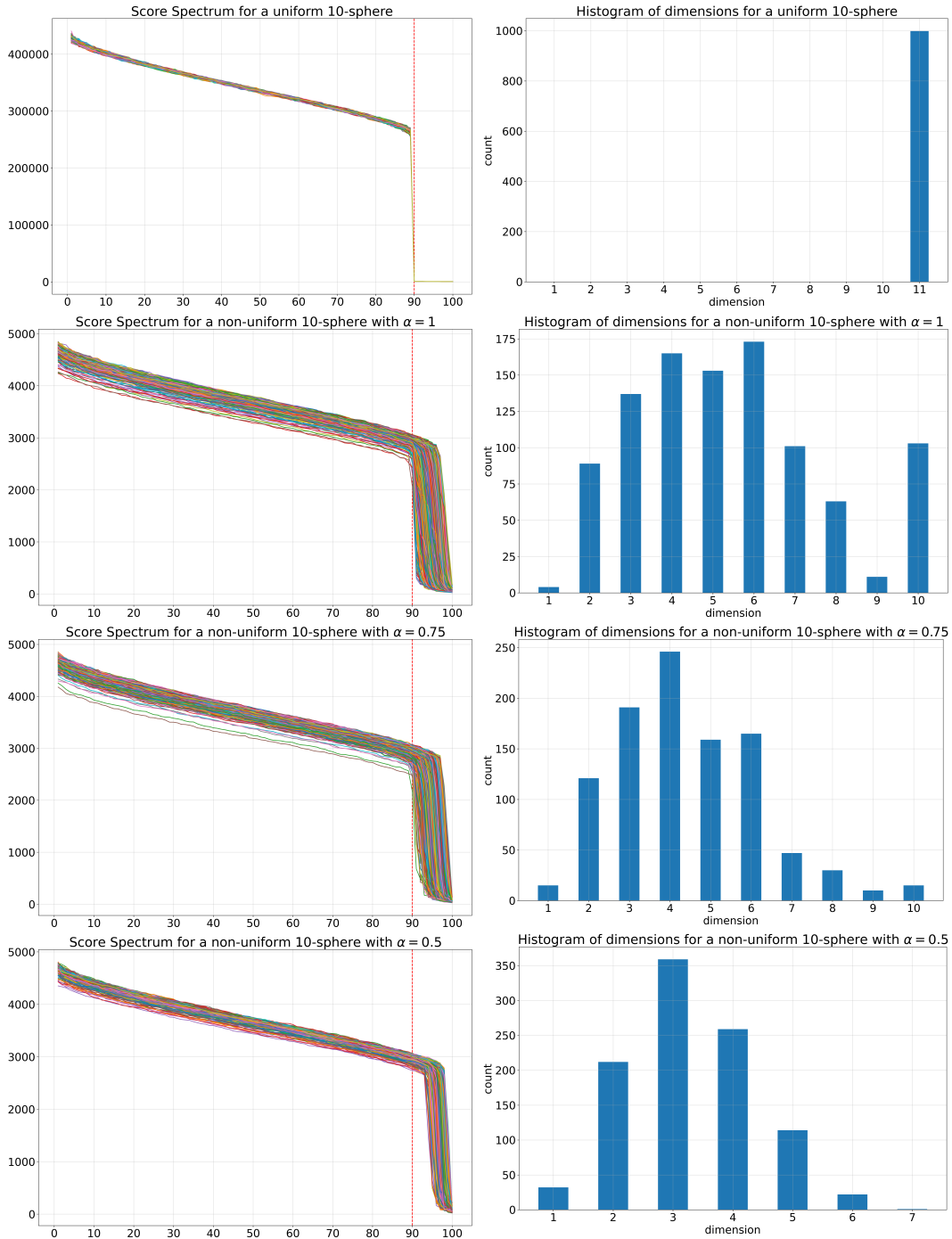


Figure 17: Dimensionality estimates for uniform and non-uniform distributions on a 10-sphere. On the right we present histograms showing how many points  $\mathbf{x}_0^{(j)}$  result in a given  $\hat{k}(\mathbf{x}_0^{(j)})$ . Taking  $\hat{k} = \max_j \hat{k}(\mathbf{x}_0^{(j)})$  allows for robust estimation for moderate values of the concentration parameter  $\alpha$ .

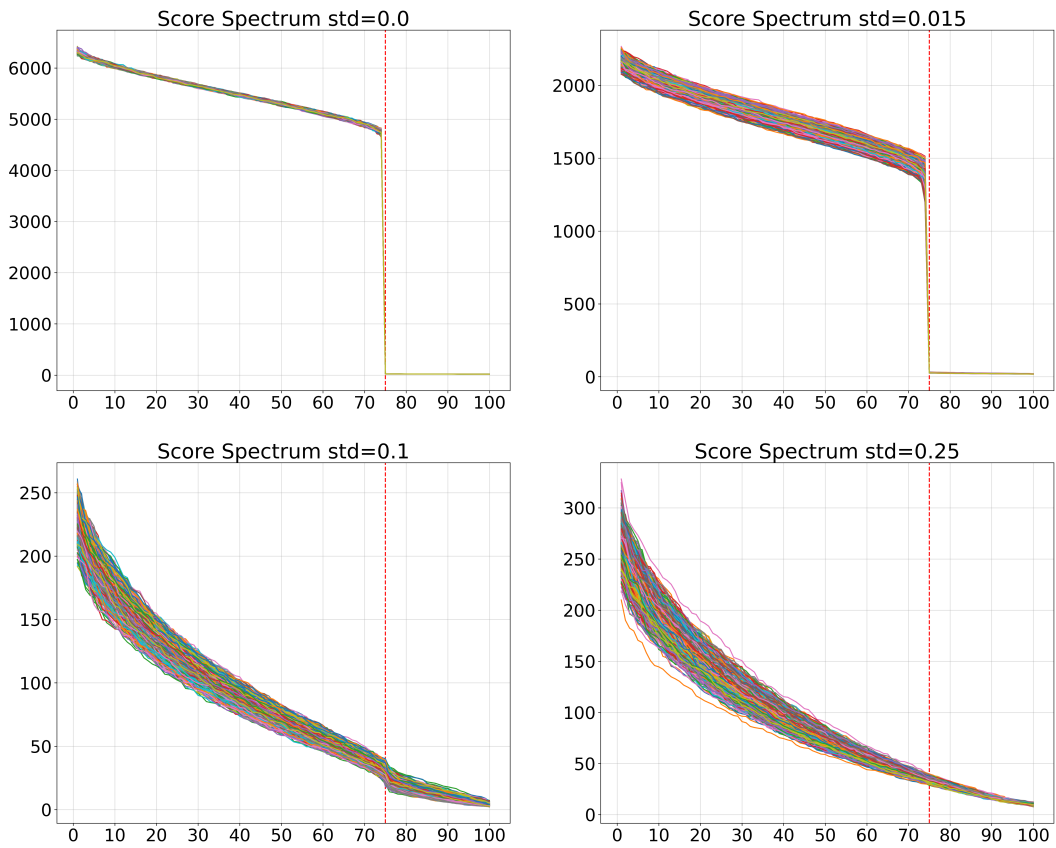


Figure 18: Score spectra for score models on 25-sphere trained on noisy manifold data.